Check for updates

Advanced Energy Materials

ADVANCED ENERGY MATERIALS
www.advenergymat.de

RESEARCH ARTICLE

Streamlined Y6-Analogs Enabling Efficient Ambient-Air-Processed Organic Solar Cells

Sung Jae Jeon[1] | Nam Gyu Yang[1] | Ji Youn Kim[1] | Eunkyung Cho[2] | Jeewon Park[3] | Geonheon Lee[3] | Changduk Yang[3,4] | Doo Kyung Moon[1]

[1]Nano, and Information Materials (NIMs) Laboratory, Department of Chemical Engineering, Konkuk University, Gwangjin-gu, Seoul, South Korea | [2]Division of Energy and Environmental Technology, DGIST, Daegu, Republic of Korea | [3]School of Energy and Chemical Engineering, Ulsan National Institute of Science and Technology (UNIST), Ulju-gun, Ulsan, South Korea | [4]Graduate School of Carbon Neutrality, Ulsan National Institute of Science and Technology (UNIST), Ulju-gun, Ulsan, South Korea

Correspondence: Doo Kyung Moon (dkmoon@konkuk.ac.kr)

Received: 10 September 2025 | **Revised:** 21 January 2026 | **Accepted:** 1 February 2026

Keywords: ambient-air process | non-fullerene acceptors | scalability | ternary organic solar cells | Y6 analogues

ABSTRACT

Achieving high efficiency and long-term stability under ambient processing conditions remains a critical hurdle for the commercialization of organic solar cells (OSCs). Here, we report two new Y6-analogs—BT(BO)-*v*-T(C12)-4F (4F) and BT(BO)-*v*-T(C12)-4Cl (4Cl)—featuring vinylene (*v*)-bridged DA′D cores, designed to improve the material's scalability while maintaining the structural advantages of Y6-type acceptors. Morphological and device-level investigations reveal that these M-Y6 derivatives facilitate thermodynamically stable molecular packing and favorable crystalline orientation, even when fully processed in air. Incorporation of 4F into a layer-by-layer ternary architecture with D18/L8-BO via a reproducible air-processing protocol results in a certified power conversion efficiency (PCE) of 19%, among the highest reported for conventional OSCs fabricated under ambient conditions. Moreover, 4F-based devices demonstrate exceptional thermal and photostability, retaining over 80% of their initial PCE after extended aging under the ISOS-L-1 protocol without encapsulation. These improvements are attributed to the enhanced crystallinity, vertical molecular alignment, and morphological robustness imparted by the 4F acceptor. This study identifies BT(BO)-*v*-T(C12)-4F as a promising air-processable acceptor for scalable OSCs that combine high efficiency with long-term operational durability.

1 | Introduction

Organic solar cells (OSCs) are emerging as promising next-generation photovoltaic technologies, offering unique advantages such as mechanical flexibility, low environmental footprint, and compatibility with scalable roll-to-roll (R2R) manufacturing methods [1–4]. While their power conversion efficiencies (PCEs) still lag behind those of silicon and perovskite solar cells, recent advances have propelled small-area OSCs past the 20% threshold, making them increasingly competitive and commercially relevant [5–10]. These performance gains have largely stemmed from innovations in the design of photoactive layers (ALs), particularly in the development of high-performance electron acceptors.

A major turning point in OSC design has been the shift from fullerene-based acceptors (e.g., $PC_{61}BM$, $PC_{71}BM$) to non-fullerene acceptors (NFAs), with Y6-type materials (e.g., L8-BO, BTP-eC9) representing the current state of the art [11, 12]. Unlike fullerene-based systems, Y6 derivatives offer multifunctionality through tailored molecular engineering—combining strong near-infrared (NIR) absorption, favorable energy level alignment, and controlled molecular packing [11]. These properties stem from

© 2026 Wiley-VCH GmbH

their planar C- or U-shaped A–DA′D–A architecture, typically built around a dithienothiophene[3,2-*b*]-pyrrolobenzothiadiazole (DTTPBT) core with strategic terminal groups and alkyl side chains [13–15]. This structural design lowers the bandgap, raises the lowest unoccupied molecular orbital (LUMO) level, and promotes face-on packing for enhanced optoelectronic performance [16].

However, a key limitation remains: the synthetic complexity and low yield of benchmark Y6-type materials. For instance, the widely used L8-BO requires 19 synthetic steps and affords only ~3.4% overall yield, posing a major bottleneck to scalable production [17]. Recent research has therefore sought to simplify NFA structures while maintaining their critical optoelectronic properties [13–15, 17–19]. For example, the replacement of complex central cores, such as the heptacyclic DTTPBT unit, with simpler pentacyclic units—specifically dithiophene-pyrrolobenzotriazole (DTPBTA) in Y26 [19] or BTA-C4-Cl [17]—has led to PCEs exceeding 16%–17%. These outcomes are comparable to those observed in Y6-based OSCs; however, they still require inert fabrication conditions.

Beyond molecular design, achieving scalable processing under ambient-air conditions has emerged as a critical objective for the practical deployment of OSCs. Most high-performance OSCs are fabricated in glovebox (GB) environments under inert conditions, limiting commercial scalability [20, 21]. Notably, high relative humidity (RH) adversely affects film morphology and device performance, particularly during the fabrication of the active layer in ambient conditions [22].

Recent efforts have addressed this through materials innovation: for example, the Chen group demonstrated stable performance using siloxane-functionalized donors like PQSi705 in humid air (~93% RH), achieving 16.1% PCE and long-term stability in unencapsulated devices [23]. Similarly, siloxane-based additives [24] and hydrophobic interfacial layers [25] have enabled PCEs approaching 19% under high-RH conditions.

Despite these advances, few studies have addressed the dual challenge of (i) reducing the synthetic complexity of NFAs and (ii) achieving high-efficiency, ambient-air-processed OSCs using a robust, reproducible protocol under variable RH conditions. Most prior studies focus on individual parameters (e.g., AL design or processing within locally humidity-controlled environments), leaving a gap in holistic strategies that combine molecular simplification with environmental processability.

In addressing this dual challenge, we have developed two structurally simplified Y6 analogs—BT(BO)-*v*-T(C12)-4F and BT(BO)-*v*-T(C12)-4Cl—featuring a unique vinylene (*v*)-linked DA′D core (Figure 1). This innovative design was implemented via a high-yield Heck coupling strategy, utilizing 5,6-bis((2-butyloctyl)oxy)benzo[*c*][1,2,5]thiadiazole (BT(BO)) as the acceptor unit and two 3-dodecylthiophene (T(C12)) segments as donor units.

These analogs retain the essential features of A–DA′D–A frameworks (planarity, energy levels, solubility) while significantly improving synthetic efficiency—requiring only 12–13 steps and yielding 5.5%–7.8%, which is notably higher than that of L8-BO. Although binary OSCs based on these acceptors achieved moderate PCEs (11.3%–12.8%), their intrinsic high crystallinity and low surface energy facilitated ternary device integration with established donor–acceptor systems (e.g., PM6:L8-BO, D18/L8-BO).

Notably, using a layer-by-layer (LBL) processed ternary strategy, devices incorporating BT(BO)-*v*-T(C12)-4F achieved a certified PCE of 19% (max 19.2%)—among the highest for ambient-air-processed OSCs. These devices were fabricated entirely in air, excluding only the top electrode step, under variable RH conditions with consistent performance. Optimization of hole transport layers (HTLs), ALs, and electron transport layers (ETLs) was systematically conducted using a robust, scalable protocol.

In summary, our work demonstrates a viable path toward high-performance, cost-effective OSCs via simplified molecular design and ambient-compatible processing. This study provides both molecular-level insights and practical engineering strategies essential for commercial OSC manufacturing.

2 | Results and Discussion

2.1 | Material Synthesis and Characterization

The synthetic routes for the two highly scalable modified Y6 (M-Y6) series, BT(BO)-*v*-T(C12)-4F and BT(BO)-*v*-T(C12)-4Cl, are outlined in Scheme S1. Both acceptors adopt the A–DA′D–A architecture and were synthesized in five steps from 4,7-dibromo-5,6-bis((2-butyloctyl)oxy)benzo[*c*][1,2,5]thiadiazole, achieving high overall yields exceeding 50%. Detailed procedures and full characterization are provided in the Supporting Information (Figures S1–S8).

A key intermediate in the synthesis is the vinylene-linked DA′D core (BT-*v*-T; M3), prepared via a Heck coupling reaction. The reaction proceeds with high stereoselectivity, yielding exclusively the *trans*- isomer, as confirmed by two characteristic vinyl proton signals at ~7.50 and 6.84 ppm in the ^{1}H NMR spectrum (Figure S3) [26]. No α-vinyl cross-coupling byproducts were detected. The reaction affords a high yield of 85.1%, which can be attributed to intramolecular non-covalent interactions (e.g., N···H, O···H) that likely stabilize the desired geometry and suppress stereoisomer formation [27]. These stabilizing interactions also facilitated straightforward purification via silica gel chromatography.

Final products were obtained through Knoevenagel condensation of aldehyde-substituted BT-*v*-T (M4) with tetrafluoro- and tetrachloro-substituted indanone-cyano (IC) end groups, yielding BT(BO)-*v*-T(C12)-4F and BT(BO)-*v*-T(C12)-4Cl in excellent yields (~95%). This synthetic step can be effectively facilitated using the eco-friendly base L-proline, as reported in recent literature.

2.2 | Theoretical Calculations

To gain molecular-level insights into the geometry and electronic properties of the M-Y6 series, density functional theory (DFT) calculations were performed using Gaussian 16 at both the B3LYP/6-31G(d) and ωB97XD/6-31G(d,p) levels of theory. The

16146840, 0, Downloaded from https://advanced.onlinelibrary.wiley.com/doi/10.1002/aenm.202505110 by Sanghuh Memorial Library, Wiley Online Library on [11/03/2026]. See the Terms and Conditions (https://onlinelibrary.wiley.com/terms-and-conditions) on Wiley Online Library for rules of use; OA articles are governed by the applicable Creative Commons License

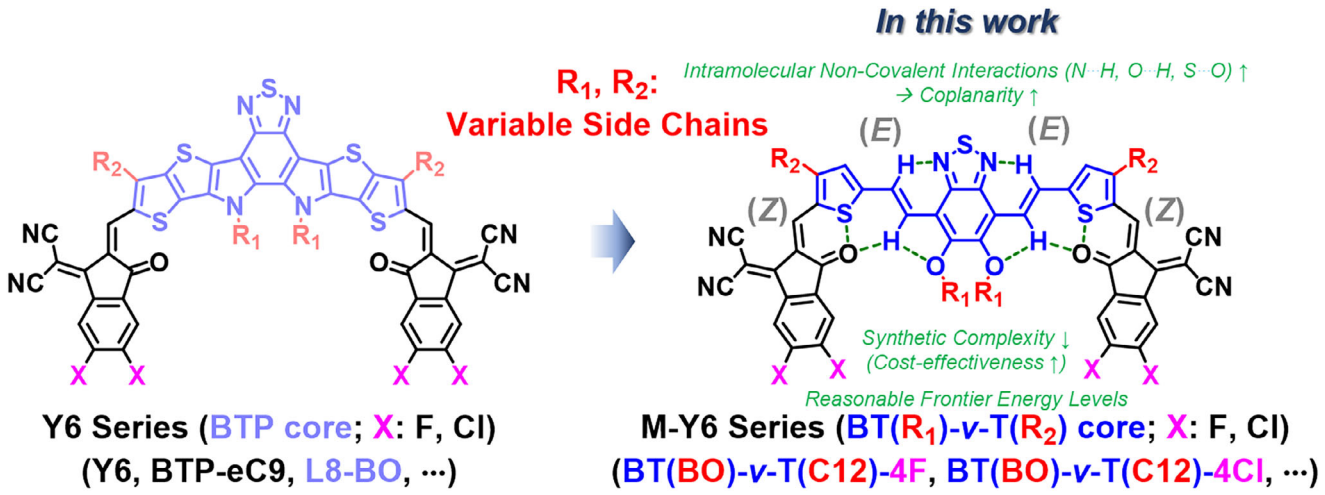

FIGURE 1 | Design strategy of the modified-Y6 (M-Y6) series, inspired by the Y6 series.

reference Y6-type molecule L8-BO and the M-Y6 analog BT(BO)-*v*-T(C12)-4F were selected for comparative analysis (Figure 2a). For computational efficiency, alkyl side chains were replaced with methyl, isobutyl, and butyl groups. Additional computational details are available in the Supporting Information.

A dihedral energy scan of the model compound M-Y6-MC1 (Figure 2b), which features simplified side chains consisting of methyl groups, revealed two energy minima at $\theta_2 \approx 0°$ and 180°, indicating thermodynamically accessible planar conformations [28]. This planarity, stabilized by intramolecular N…H and O…H interactions and vinylene linkages [28–32], supports the formation of C- or U-shaped backbones similar to those in typical Y6-type architectures [11, 16].

To gain deeper structural insight, the alkyl side chains were simplified to isobutyl and butyl groups in the DFT-optimized geometries of M-Y6-MC2 (4F) and Y6-MC2 (L8-BO). The resulting structures (Figure 2c) reveal that M-Y6-MC2 (4F) adopts a nearly planar conformation, with a total dihedral angle (θ_{total}) of 7.52°, which is comparable to that of Y6-MC2 (L8-BO) (1.44°), indicating preserved backbone planarity despite the structural simplification. Despite being slightly less planar, M-Y6-MC2 (4F) exhibits a smaller backbone tilting angle (10° vs. 15°), suggesting increased rigidity—an attribute favorable for charge transport [11, 33]. Notably, M-Y6-MC2 (4F) also displays a significantly larger dipole moment (2.36 D) compared to Y6-MC2 (L8-BO) (0.08 D), potentially enhancing dipole–dipole interactions and promoting charge carrier mobility in OSC devices [7, 11, 17, 31, 33].

Frontier molecular orbital analysis revealed similar highest occupied molecular orbital (HOMO) levels (−5.555 eV for M-Y6-MC2 (4F) vs. −5.585 eV for Y6-MC2 (L8-BO)), indicating comparable electron-donating behavior. However, M-Y6-MC2 (4F) exhibits a deeper LUMO level (−3.659 eV vs. −3.524 eV), attributed to increased delocalization over the benzothiadiazole moiety, resulting in a narrower calculated bandgap (1.896 eV vs. 2.061 eV). These findings suggest improved light-harvesting capabilities, which are consistent with time-dependent DFT results (Figure S11).

To evaluate electrostatic surface features, electrostatic potential (ESP) maps on van der Waals surfaces were generated (Figure 2d) [17, 32, 33]. Both M-Y6-MC2 (4F) and Y6-MC2 (L8-BO) exhibit localized electronegative regions around fluorine, carbonyl, and cyano groups. However, Y6-MC2 (L8-BO) displays a more concentrated positive ESP in the DA′D core, reflected in its average positive ESP (7 kcal mol^{-1} vs. 5.17 kcal mol^{-1} for M-Y6-MC2, Figure 2e; Figure S12). While this lower ESP in M-Y6-MC2 (4F) may reduce interfacial electric field formation with donor polymers, its broader positive ESP distribution on the benzothiadiazole ring could enhance donor–acceptor charge separation through favorable π–π interactions [31–33].

Similar trends were observed in M-Y6-MC2 (4Cl), incorporating tetrachloro-substituted IC end groups. This variant exhibited further improvements in dipole moment, HOMO level alignment, bandgap narrowing, and ESP characteristics due to the chlorination effect (Figures S12–S14) [34]. Key computational parameters are summarized in Table S1. These results have been further validated by cross-checking the DFT calculations using two different computational methods (Figures S15–S16 and Table S2).

To validate the presence of intramolecular non-covalent interactions (e.g., N···H and O···H) hypothesized to promote molecular planarity and thermodynamic stability, we conducted reduced density gradient (RDG) analysis on the DFT-optimized geometries of M-Y6-MC2 (4F), M-Y6-MC2 (4Cl), and Y6-MC2 (L8-BO) [35]. The RDG results confirm the presence of localized attractive interactions in M-Y6-MC2 (4F) and M-Y6-MC2 (4Cl)—absent or weaker in Y6-MC2 (L8-BO)—supporting our interpretation that such interactions contribute to the planar backbone and high trans-isomer selectivity of the M-Y6 series (Figure S17).

To investigate the preferential molecular packing structures of the M-Y6 series, we optimized three representative dimer configurations with varying degrees of backbone overlap using DFT calculations at the ωB97XD/6-31G** level of theory. Dimer 1 (T–T; terminal-to-terminal), Dimer 2 (CT–CT; core-to-terminal), and Dimer 3 (whole–whole; full backbone overlap) represent

16146840, 0, Downloaded from https://advanced.onlinelibrary.wiley.com/doi/10.1002/aenm.202505110 by Sanghuh Memorial Library, Wiley Online Library on [11/03/2026]. See the Terms and Conditions (https://onlinelibrary.wiley.com/terms-and-conditions) on Wiley Online Library for rules of use; OA articles are governed by the applicable Creative Commons License

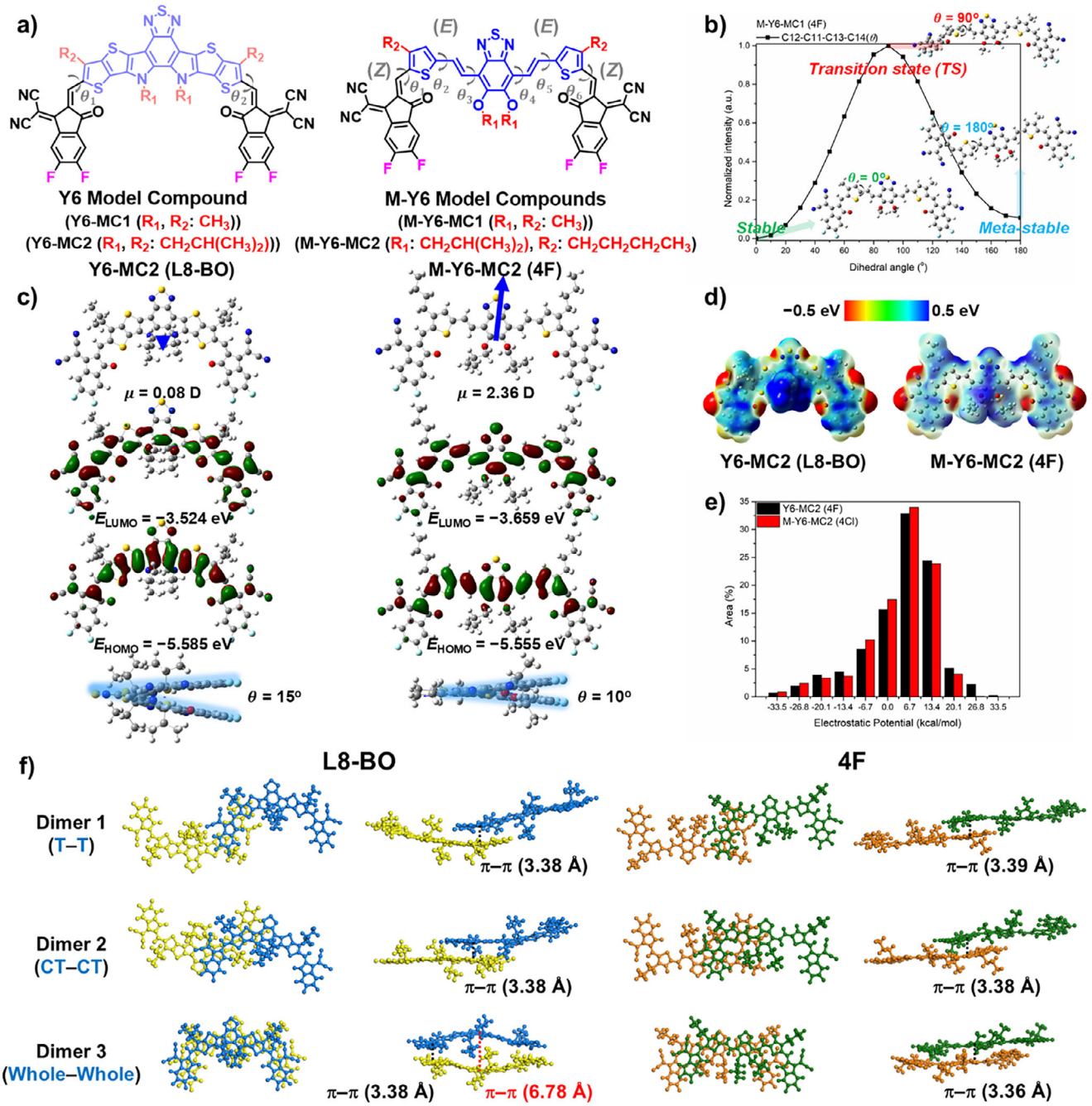

FIGURE 2 | (a) Molecular structures of the model compounds for L8-BO (Y6-MC1 and Y6-MC2) and BT(BO)-*v*-T(C12)-4F (M-Y6-MC1 and M-Y6-MC2). (b) Normalized potential energy scan results for M-Y6-MC1 as a function of the dihedral angle (θ_2). (c–e) DFT calculation results of Y6-MC1 and M-Y6-MC2: (c) Top view, LUMO and HOMO distributions, side view; (d) ESP surface; and (e) ESP area distribution diagram of the corresponding model compounds. (f) Dimer configurations of the model compounds for L8-BO and 4F.

configurations with approximately one-third, one-half, and full overlap of the conjugated backbones, respectively (Figure 2f; Table S3). Among these, Dimer 1 and Dimer 2 correspond to π–π stacking motifs previously observed in single-crystal structures of Y6-type acceptors and consistently reproduced in molecular dynamics simulations [36, 37].

Despite extensive crystallization attempts, high-quality single crystals suitable for single-crystal X-ray diffraction (SC-XRD) analysis could not be obtained, likely due to the high solubility and conformational flexibility conferred by the long dodecyl side chains of the M-Y6 series.

The M-Y6 dimers maintain strong π–π stacking interactions (3.36–3.39 Å) across all three configurations, reinforcing the molecular design's intrinsic propensity for stacking. Notably, Dimer 3, which features full backbone overlap, exhibits the lowest binding and interaction energies, indicating that it is the most thermodynamically favorable configuration. Our calculations further show that this preference holds for both planar

16146840, 0, Downloaded from https://advanced.onlinelibrary.wiley.com/doi/10.1002/aenm.202505110 by Sanghuh Memorial Library, Wiley Online Library on [11/03/2026]. See the Terms and Conditions (https://onlinelibrary.wiley.com/terms-and-conditions) on Wiley Online Library for rules of use; OA articles are governed by the applicable Creative Commons License

conformations of the terminal thiophene side chains (torsion angles of 0° and 180°; see Figures S18–S19 and Table S4), suggesting a conformationally robust packing mode. The fully overlapped π–π stacking geometry of Dimer 3 facilitates an edge-on molecular orientation, which is additionally stabilized by the long alkyl side chains that promote out-of-plane packing. Such packing not only enhances cohesive energy density but also promotes vertical charge transport pathways, potentially improving device performance if long-range order is induced during film formation.

In contrast, Dimer 3 is unlikely to form for L8-BO due to steric hindrance from its core side chains, which disrupt π–π interactions (6.78 Å) of the core-to-core. While Dimer 3 still shows the lowest calculated binding energy, its formation is sterically disfavored. Instead, L8-BO exhibits comparable binding energies for Dimer 1 and Dimer 2, suggesting that both configurations are energetically accessible and likely coexist—consistent with previous experimental observations [36, 37].

These results highlight how modest structural modifications derived from the vinylene linkage can profoundly affect the molecular packing landscape of Y6-type acceptors. While M-Y6 supports dense, edge-on packing via full-backbone π–π overlap, L8-BO prefers compact face-on orientation due to its intrinsic packing modes. This dichotomy not only influences the degree of crystallinity and molecular orientation in thin films but also impacts key optoelectronic parameters such as charge mobility, exciton diffusion length, and morphological stability.

2.3 | Physical, Optical, and Electrochemical Properties

To balance solubility and aggregation, the M-Y6 series was designed with 2-butyloctyl branched alkoxy chains on the central BT unit and linear dodecyl chains on the outer thiophenes. As a result, both BT(BO)-*v*-T(C12)-4F (hereafter 4F) and BT(BO)-*v*-T(C12)-4Cl (hereafter 4Cl) exhibited good solubility in chloroform (CF) and carbon disulfide (CS_2) under mild heating. However, their solubility in chlorobenzene (CB) at room temperature (RT) was limited, requiring temperatures >100°C to dissolve—reflecting strong intermolecular aggregation. Solubility in hot CB follows the trend: L8-BO > 4F > 4Cl.

The thermal properties of the M-Y6 acceptors were examined using thermogravimetric analysis (TGA) and differential scanning calorimetry (DSC). As shown in Figure S20, 4F and 4Cl exhibit excellent thermal stability, with 5% weight loss temperatures of 308.1°C and 306.4°C, respectively. DSC curves revealed a melting temperature (T_m) of 269.7°C for 4F, while 4Cl exhibited two distinct melting transitions at 273.1°C and 280.6°C (Figure S21). The dual melting behavior observed in 4Cl may originate from thermally induced recrystallization–remelting events or polymorphic transitions between distinct molecular packing motifs, as supported by variable-temperature GIWAXS measurements (discussed later) [38–40]. Further investigation using SC-XRD analysis is warranted to fully resolve the structural basis for this behavior. While slightly lower than L8-BO (319°C), the melting enthalpies of 4F (−39.2 J g^{-1}) and 4Cl (−37.4 J g^{-1}; sum of both peaks at 273.1°C and 280.6°C) are comparable or even higher than L8-BO (−38.6 J g^{-1}), indicating strong crystalline order, essential for efficient charge transport [12, 38, 39].

UV–vis absorption spectra were recorded in solution and thin films (Figures S22–S24). In solution, 4F and 4Cl displayed slightly lower maximum absorption peaks (λ_{max}^{sol}s) at 683 nm (ε_{max}^{sol} = 1.31 × 10^5 M^{-1} cm^{-1}) and 695 nm (ε_{max}^{sol} = 1.11 × 10^5 M^{-1} cm^{-1}), respectively, compared to 731 nm for L8-BO (ε_{max}^{sol} = 1.90 × 10^5 M^{-1} cm^{-1}): The maximum extinction coefficients (ε_{max}^{sol}s) in parentheses were calculated using the Beer–Lambert law for various diluted solutions [28, 31]. Upon film formation, red shifts of 64 nm (4F) and 60 nm (4Cl) were observed, along with vibronic shoulders, indicative of strong intramolecular charge transfer (ICT) and intermolecular interactions [14, 17, 22, 28]. The optical bandgaps (E_g^{opt}s) were estimated as 1.50 eV (4F) and 1.49 eV (4Cl), slightly wider than L8-BO (1.40 eV), suggesting reduced NIR absorption.

Electrochemical analysis via cyclic voltammetry (CV) (Figure S25) revealed HOMO/LUMO energy levels (E_{HOMO}/E_{LUMO}) of −5.84/−3.96 eV (4F) and −5.90/−3.99 eV (4Cl), which are slightly deeper than those of L8-BO (−5.65/−3.91 eV). This shift may influence open-circuit voltage (V_{OC}) and charge transfer dynamics in OSC devices [13, 31]. These parameters are consistent with the trends observed in DFT calculations.

Notably, the slightly reduced optical properties of the M-Y6 series, compared to DFT predictions, may result from weaker push–pull effects or less favorable packing in the solid state [12, 31]. Nonetheless, the M-Y6 acceptors retain key traits such as crystallinity, thermal robustness, and film-forming ability that are essential for OSC applications. A summary of key optical and electrochemical parameters is provided in Table 1.

2.4 | Photovoltaic Performances

To evaluate the photovoltaic properties of the M-Y6 series, we fabricated OSCs using conventional device architectures: ITO/HTL(PEDOT: PSS or PEDOT: PSS/Cl-2PACz)/AL-/ETL(PDINN or PDIN)/Ag. Device configurations included both binary blends (PM6:M-Y6) and air-processed ternary blends (PM6:L8-BO: M-Y6 and D18/L8-BO: M-Y6), as illustrated in Figure 3a.

PM6 was selected to establish a baseline for compatibility and performance benchmarking with the newly developed M-Y6 NFAs, while D18 was employed in the D18/L8-BO: M-Y6 ternary system to explore efficiency enhancement via NFA incorporation in state-of-the-art donor systems.

As shown in Figure 3b, despite lower ε_{max}^{sol}s of M-Y6 acceptors, their film-state absorption coefficients (ε_{max}^{film}s) remain comparable to L8-BO (1.39 × 10^5 cm^{-1}), reaching 1.23 × 10^5 cm^{-1} (4F) and 1.14 × 10^5 cm^{-1} (4Cl). Both M-Y6 acceptors exhibited mixed J- and H-aggregation, with 4Cl favoring H-aggregation and L8-BO exhibiting dominant J-aggregation. These aggregation characteristics are expected to enable complementary absorption and favorable molecular ordering when incorporated into ternary blends with PM6:L8-BO or D18/L8-BO (Figure 3c) [32, 41, 42].

16146840, 0, Downloaded from https://advanced.onlinelibrary.wiley.com/doi/10.1002/aenm.202505110 by Sanghuh Memorial Library, Wiley Online Library on [11/03/2026]. See the Terms and Conditions (https://onlinelibrary.wiley.com/terms-and-conditions) on Wiley Online Library for rules of use; OA articles are governed by the applicable Creative Commons License

TABLE 1 | Optical and electrochemical properties of the M-Y6 series with L8-BO.

Materials	λ_{max}^{sol} (nm)	ε_{max}^{sol} ($\times 10^5$; M^{-1} cm^{-1})	λ_{max}^{film} (nm)	ε_{max}^{film} ($\times 10^5$; cm^{-1})	E_g^{opt}[a] (eV)	E_{HOMO}[b] (eV)	E_{LUMO}[b] (eV)
BT(BO)-*v*-T(C12)-4F	683 (@ *0–0*)	1.31 (@ 683 nm)	678 (−5; @ *0–1*), 747 (+64; @ *0–0*), 681 (−2; @ *0–1*)[c], 750 (+67; @ *0–0*)[c]	1.23 (@ 678 nm), 1.20 (@ 747 nm)	1.50, 1.49[c]	−5.84	−3.96
BT(BO)-*v*-T(C12)-4Cl	695 (@ *0–0*)	1.11 (@ 695 nm)	682 (−13; @ *0–1*), 755 (+60; @ *0–0*), 693 (−3; @ *0–1*)[c], 764 (+69; @ *0–0*)[c]	1.14 (@ 682 nm), 0.95 (@ 755 nm)	1.49, 1.48[c]	−5.90	−3.99
L8-BO	731 (@ *0–0*)	1.90 (@ 731 nm)	805 (+74; @ *0–0*)	1.39 (@ 805 nm)	1.40	−5.65	−3.91

[a] $E_g^{opt} = 1240/\lambda_{onset}^{film}$ (λ_{onset}^{film}s were calculated from the intersection of the tangent on the low energetic edge of the absorption spectrum with the baseline).
[b] $E_{HOMO\ or\ LUMO} = -4.8 - [E_{ox\ or\ red}^{onset}$ (vs. Ag/AgCl) − $E_{1/2}$(Fc/Fc$^+$ vs. Ag/AgCl)] ($E_{1/2}$(Fc/Fc$^+$ vs. Ag/AgCl) = 0.48 eV).
[c] These values were calculated from the films using a mixed solvent of CF and CS_2.

Furthermore, the energy level alignment among the donors (PM6 or D18) and acceptors (L8-BO and M-Y6) forms favorable cascaded architectures, facilitating efficient exciton dissociation and promoting directional charge transport (Figure 3d; Figure S26) [16, 25, 31, 32, 34, 43].

While the control device PM6:L8-BO achieved a PCE of 16.9%, the binary OSCs (PM6:M-Y6), fabricated under nitrogen (N_2) GB conditions, exhibited moderate PCEs of 12.8% (4F) and 11.3% (4Cl). This performance gap may be primarily attributed to the reduced near-infrared absorption and suboptimal molecular orientation in the M-Y6 series, which limit photon harvesting and vertical charge transport. Full optimization procedures and detailed fabrication parameters are provided in Figure 3e and Tables S5–S6. Notably, despite having deeper LUMO levels, the V_{OC} of 4F-based devices (0.878 V) was comparable to that of L8-BO-based references (0.871 V) (Table S7). This finding suggests that our DA′D core modification supports high V_{OC} values similar to those achieved with L8-BO.

In contrast, the lower performance of 4Cl-based devices was primarily due to reduced short-circuit current density (J_{SC}) and fill factor (FF), suggesting that the incorporation of tetrachloro end groups may adversely affect charge generation or transport within this backbone design. These observations were corroborated by external quantum efficiency (EQE) measurements, which revealed suppressed photocurrent response for 4Cl devices compared to their 4F counterparts.

To further enhance light harvesting and active layer performance, M-Y6 acceptors were introduced as third components in ternary OSCs, processed entirely in ambient air (except for the top electrode). This fabrication strategy reflects industrially relevant conditions and demonstrates the robustness of the M-Y6 series under practical manufacturing environments [22, 25, 42]. To streamline the main text, extended PM6-based ternary device data and optimization results have been moved to the Supporting Information. Only key findings relevant to mechanistic understanding are retained here.

To ensure high reproducibility under ambient processing, we systematically optimized the interfacial layers (HTL and ETL) alongside the active layer. For HTL, humidity-tolerant PEDOT:PSS films were achieved via DI water dilution, while ETL performance was maximized by tuning PDINN or PDIN formulations in various solvents. These optimizations led to PCEs approaching those of glovebox-processed counterparts (Table S7). The more detailed notes were summarized in the Supporting Information.

Building upon this foundation, air-processed ternary OSCs based on the PM6:L8-BO system were fabricated by incorporating M-Y6 acceptors as third components. Both PM6:L8-BO:4F and PM6:L8-BO:4Cl ternary devices demonstrated clear performance enhancement compared to the binary control (16.6%), reaching PCEs of 17.4% and 16.8%, respectively. In particular, the 4F-based ternary blend notably improved J_{SC} and EQE across the full spectral range (Figure S27). Comprehensive device optimization procedures and full performance datasets are provided in the Supporting Information (Tables S8–S10).

To overcome the morphological limitations of single-step BHJ processing—such as excessive donor–acceptor mixing and poor vertical phase separation—we adopted an LBL strategy to fabricate ternary D18/L8-BO: M-Y6 devices under ambient air. This architecture supports the formation of pseudo-bilayer structures with favorable vertical composition gradients, promoting enhanced charge transport and morphological order under practical conditions [7, 9, 44, 45].

Prior to ternary fabrication, we optimized the electron and hole transport layers (ETL and HTL) for D18/L8-BO binary devices under ambient RH conditions. Notably, PDIN-based ETLs enabled PCEs up to 17%, comparable to glovebox-processed controls (17.3%). We also found that HTL formulation plays a crucial role in mitigating RH-induced performance losses: while diluted PEDOT:PSS improves interface quality and device efficiency under low RH by offering better wettability, uniformity, and reduced acidity, pristine PEDOT:PSS becomes more effective at RH > 60%, likely due to its denser polymer

16146840, 0, Downloaded from https://advanced.onlinelibrary.wiley.com/doi/10.1002/aenm.202505110 by Sanghuh Memorial Library, Wiley Online Library on [11/03/2026]. See the Terms and Conditions (https://onlinelibrary.wiley.com/terms-and-conditions) on Wiley Online Library for rules of use; OA articles are governed by the applicable Creative Commons License

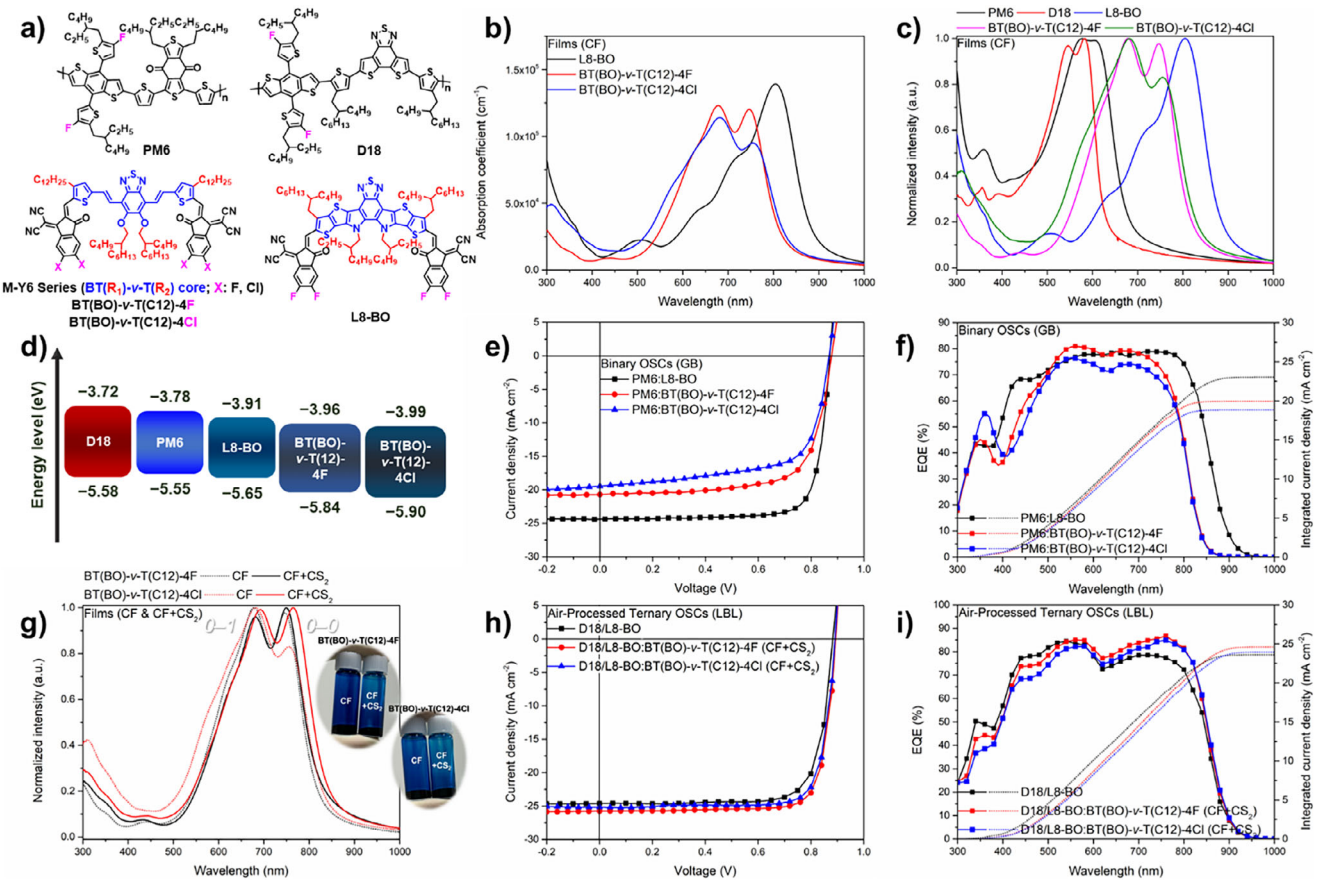

FIGURE 3 | (a) Molecular structures of the active materials used in this study. (b) Absorption coefficients in the film state for L8-BO, BT(BO)-*v*-T(C12)-4F, and BT(BO)-*v*-T(C12)-4Cl. (c) Normalized absorption spectra and (d) energy-band diagram of the active materials in the film state. (e) *J*–*V* and (f) EQE curves for binary OSCs (GB) based on PM6:NFA blends. (g) Normalized absorption spectra of the M-Y6 series under different solvent conditions: CF and a mixture of CF and CS_2 (CF: CS_2 = 8:2; v/v). (h) *J*–*V* and (i) EQE curves for air-processed ternary OSCs (LBL) based on D18/L8-BO, incorporating M-Y6 acceptors, processed using a mixed solvent of CF + CS_2 (8:2 v/v).

network and thicker film coverage that enhance resistance to moisture-induced degradation and preserve interface integrity.

These optimizations ensured robust baseline performance and were critical for achieving stable and efficient ternary devices. Full datasets and environmental tolerance analyses are presented in the Supporting Information (Table S11).

Building upon the optimized device architecture, LBL-processed ternary OSCs based on D18/L8-BO were fabricated under ambient air conditions (RH < 40%) by incorporating M-Y6 acceptors as third components. The optimized acceptor ratios—L8-BO:4F = 9:1 and L8-BO:4Cl = 9:1—were consistent with those used in the BHJ ternary systems (i.e., L8-BO:4F = 0.9:0.1 and L8-BO:4Cl = 0.9:0.1 by weight). As shown in Figure S28, the LBL-processed ternary devices achieved PCEs of 18.3% for 4F and 17.4% for 4Cl, both exceeding that of the binary control device (17%). These results underscore the advantages of the LBL approach in facilitating vertical phase separation, improving interfacial coherence, and enabling more efficient charge transport pathways, thereby delivering superior performance compared to the conventional BHJ configuration.

The optical properties of the M-Y6 acceptors were further optimized through solvent engineering by introducing a CF: CS_2 (8:2 v/v) co-solvent system in place of neat CF. As shown in Figure 3g and Figures S29–S30, this modification induced notable red-shifts in the film-state absorption maxima (λ_{max}^{film}s), a slight narrowing E_g^{opt}s from 1.50 to 1.49 eV for 4F and from 1.49 to 1.48 eV for 4Cl, and an increased intensity ratio between the 0–0 and 0–1 vibrational transitions (I_{0-0}/I_{0-1})—indicative of enhanced NIR absorption and stronger J-type aggregation (Table 1) [28, 44].

These improvements in the solid-state photophysical characteristics translated directly to superior device performance. Specifically, ternary OSCs processed with the CF: CS_2 solvent system achieved significantly higher PCEs of 18.6% (4F) and 18% (4Cl), as shown in Figure 3h. The efficiency gains are primarily attributed to the boosted EQE responses within the 600–900 nm spectral region (Figure 3i; Figure S31), highlighting the critical role of solvent-induced molecular organization in optimizing light harvesting and photocurrent generation. Comprehensive device optimization procedures and full performance datasets are summarized in Tables S12 and S13.

To further enhance the photovoltaic performance of 4F-based ternary devices (CF + CS_2), we implemented a bilayer HTL strategy. This approach combined a diluted PEDOT: PSS layer with various self-assembled monolayers (SAMs), 2PACz derivatives, to facilitate efficient interfacial charge extraction and

16146840, 0, Downloaded from https://advanced.onlinelibrary.wiley.com/doi/10.1002/aenm.202505110 by Sanghuh Memorial Library, Wiley Online Library on [11/03/2026]. See the Terms and Conditions (https://onlinelibrary.wiley.com/terms-and-conditions) on Wiley Online Library for rules of use; OA articles are governed by the applicable Creative Commons License

improve film uniformity under ambient processing conditions. Detailed fabrication procedures are provided in the Supporting Information.

As summarized in Table S14, devices incorporating 2PACz, Cl-2PACz, and Br-2PACz achieved PCEs of 18.5%, 18.8%, and 18.7%, respectively, under RH < 40%. Halogenated variants, particularly Cl-2PACz, exhibited superior reproducibility and air-processability, likely due to enhanced monolayer coverage and interfacial compatibility. Importantly, the bilayer HTL structure enabled stable performance across a wide range of humidity conditions (RH = 33–58%). At RH = 44%, the PCE slightly declined to 18.5%, but subsequently recovered to 18.9% by increasing Cl-2PACz concentration. Even at RH = 58%, devices retained high PCEs of 18.9%, and under elevated humidity (RH = 58%), they significantly outperformed those using pristine PEDOT: PSS in terms of shelf-life stability (Figure S32).

This humidity resilience is attributed to the complementary functions of the bilayer HTL. The diluted PEDOT: PSS is considered to enhance film uniformity and surface wettability while reducing acidity-induced ITO degradation under dry conditions. In contrast, the dense Cl-2PACz layer is believed to offer superior moisture resistance, suppress interfacial void formation, and stabilize interfacial electrical properties under humid environments. These synergistic effects effectively mitigate humidity-induced performance losses often observed in single-layer PEDOT: PSS systems.

Crucially, the champion device fabricated at RH = 33% achieved a certified PCE of 19% (maximum 19.2%), with a V_{OC} of 0.890 V, J_{SC} of 26.49 mA cm^{-2}, and FF of 81.2% (Figures S33–S34, Table S15). This places it among the highest-performing conventional OSCs fabricated entirely under ambient air (excluding the top electrode) [6, 22–25, 46–50]. The excellent EQE values—88% for the donor and 87% for the acceptor—contributed substantially to the high J_{SC}, and the integrated current densities (J_{cal}) closely matched those from *J–V* measurements, with discrepancies below 5%, confirming device reliability.

Overall, these results demonstrate the strong compatibility of the 4F acceptor with the LBL architecture, delivering clear performance gains over binary systems. The PEDOT: PSS/Cl-2PACz bilayer HTL further improves device stability and humidity tolerance under ambient conditions. Together, these strategies advance the environmental robustness and scalability of OSCs for practical solar energy applications. A summary of the optimized device performances is provided in Table 2.

2.5 | Charge Transfer and Mobility Analysis

To elucidate exciton dissociation and charge transfer dynamics, steady-state photoluminescence (PL) measurements were conducted on neat and blend films [15, 17, 28, 31]. PL quenching (PLQ) efficiencies and relevant energy offsets are summarized in Tables S16–S18.

As shown in Figure S35, under 540 nm excitation, the donor-to-blend PLQ efficiencies ($PLQ_{D\to B}$) for PM6:4F and PM6:4Cl reached 99.56% and 99.20%, respectively—surpassing that of the control PM6:L8-BO blend (97.81%, Figure S36)—indicating highly efficient hole transfer from donor to acceptor.

In contrast, upon excitation at the acceptors' absorption maxima, the acceptor-to-blend PLQ efficiencies ($PLQ_{A\to B}$) were notably lower: 74.64% for 4F and 61.83% for 4Cl, compared to 97.17% for L8-BO (Figure S36). These results indicate that while hole transfer is efficient in M-Y6 systems, electron transfer is relatively limited, correlating with the reduced J_{SC} values observed in M-Y6-based binary device measurements.

The reduced $PLQ_{A\to B}$ may also point to less efficient exciton diffusion or lower probability of exciton migration into ordered domains where intermolecular charge transfer states form—a factor previously reported to impact charge separation efficiency in non-fullerene acceptor systems [51].

In contrast, BHJ-based ternary blends incorporating M-Y6 acceptors into the PM6:L8-BO system showed notable improvements in both donor- and acceptor-side photoluminescence quenching efficiencies. Specifically, $PLQ_{D\to B}/PLQ_{A\to B}$ values increased to 99.01%/98.29% for PM6:L8-BO:4F and 98.97%/97.01% for PM6:L8-BO:4Cl, compared to 97.81%/97.17% in the PM6:L8-BO binary control. These enhancements suggest that the addition of M-Y6 acceptors promotes stronger intermolecular electronic coupling, potentially enabling efficient intermolecular charge transfer or excimer-mediated charge generation mechanisms, as previously reported [52].

A similar trend was observed in LBL-based ternary blends using the D18/L8-BO system (Figure S37), where $PLQ_{D\to B}/PLQ_{A\to B}$ values increased from 99.52%/97.02% (binary control) to 99.60%/97.92% (D18/L8-BO:4F) and 99.54%/97.63% (D18/L8-BO:4Cl). These results further support the role of M-Y6 acceptors in enhancing exciton dissociation and charge transfer through favorable intermolecular interactions at well-defined donor–acceptor interfaces [51, 52].

Notably, the highest PLQ efficiencies were achieved when using the CF: CS_2 (8:2 v/v) co-solvent system, reaching 99.71%/98.50% for 4F and 99.60%/98.11% for 4Cl. These values are consistent with the enhanced J_{SC} observed in photovoltaic measurements and align well with the energy level offsets derived from CV.

The improved charge separation in these LBL blends is further facilitated by cascade-like energy level alignment between donors and acceptors (Figure S38) [31, 49], which supports directional charge transport while suppressing recombination. Unlike BHJ systems, where randomly mixed phases may promote charge back-transfer and recombination, the well-structured interfaces in LBL architectures provide a more controlled environment for efficient exciton migration, dissociation, and charge collection [43–45].

To evaluate charge transport, electron (μ_e) and hole (μ_h) mobilities, along with their balance ratio (μ_e/μ_h), were extracted via space–charge-limited current (SCLC) measurements from electron-only and hole-only devices (Figures S39–S41 and Tables S19–S21) [28, 31]. In binary blends, PM6:4F showed higher mobilities ($\mu_e = 5.12\times10^{-4}$ cm^2 V^{-1} s^{-1}, $\mu_h = 2.26\times10^{-4}$ cm^2 V^{-1}s^{-1}, and $\mu_e/\mu_h = 2.26$) compared to PM6:4Cl ($\mu_e = 4.51\times10^{-4}$ cm^2 V^{-1} s^{-1},

16146840, 0, Downloaded from https://advanced.onlinelibrary.wiley.com/doi/10.1002/aenm.202505110 by Sanghuh Memorial Library, Wiley Online Library on [11/03/2026]. See the Terms and Conditions (https://onlinelibrary.wiley.com/terms-and-conditions) on Wiley Online Library for rules of use; OA articles are governed by the applicable Creative Commons License

TABLE 2 | Photovoltaic performance of optimized binary and ternary OSCs in ambient air.

Active layer	Condition	V_{OC} [V]	J_{SC} [mA cm^{-2}]	J_{cal} [mA cm^{-2}]	FF [%]	PCE$_{max}$[a] [%]
PM6:BT(BO)-*v*-T(C12)-4F[b]	D_1:A_1	0.878	20.72	19.94	70.3	12.8 (12.4 ± 0.32)
PM6:BT(BO)-*v*-T(C12)-4Cl[b]		0.868	19.45	18.83	66.8	11.3 (10.8 ± 0.44)
PM6:L8-BO		0.870	23.99	23.04	79.7	16.6 (16.4 ± 0.17)
PM6:L8-BO:BT(BO)-*v*-T(C12)-4F	D_1:A_1:A_2	0.872	25.01	24.46	79.9	17.4 (17.1 ± 0.28)
PM6:L8-BO:BT(BO)-*v*-T(C12)-4Cl		0.869	24.26	23.69	79.4	16.8 (16.5 ± 0.29)
D18/L8-BO	D_1/A_1	0.883	24.61	23.62	78.3	17.0 (16.8 ± 0.18)
D18/L8-BO:BT(BO)-*v*-T(C12)-4F	D_1/A_1:A_2	0.891	25.55	24.58	80.3	18.3 (18.0 ± 0.20)
D18/L8-BO:BT(BO)-*v*-T(C12)-4F[c)]		0.894	25.75	24.64	80.7	18.6 (18.2 ± 0.23)
D18/L8-BO:BT(BO)-*v*-T(C12)-4F[c,d]		0.890	26.49	25.23	81.2	19.2 (18.8 ± 0.19)
D18/L8-BO:BT(BO)-*v*-T(C12)-4F[c–e]		0.887	26.586	—	80.552	19.004
D18/L8-BO:BT(BO)-*v*-T(C12)-4Cl		0.887	24.54	23.73	79.9	17.4 (17.1 ± 0.21)
D18/L8-BO:BT(BO)-*v*-T(C12)-4Cl[c]		0.891	25.18	23.97	80.4	18.0 (17.7 ± 0.24)

[a)]The average PCE values with standard deviations in parentheses were obtained from 8 individual cells.
[b)]The devices were fabricated in an N_2 GB.
[c)]The acceptor solutions were processed using a mixed solvent of CF and CS_2.
[d)]The HTL layer was utilized as a bilayer of PEODT: PSS/Cl-2PACz instead of a monolayer of PEDOT: PSS.
[e)]The certified result (TP–NC–25S–0199) was obtained from the Daegu Technopark Nanotechnology Processing Center in Korea.

μ_h = 1.73 × 10^{-4} cm^2 V^{-1} s^{-1}, and μ_e/μ_h = 2.60), reflecting higher charge imbalance and less efficient hole transport in the 4Cl-based system.

When integrated into a PM6:L8-BO-based BHJ ternary system, both 4F- and 4Cl-containing devices exhibited enhanced charge transport compared to the binary control, consistent with their improved device performance.

Notably, the enhancement was more pronounced in LBL-based ternary devices using the D18/L8-BO platform, where both M-Y6 acceptors significantly improved charge mobilities relative to the control ($\mu_e = 5.94 \times 10^{-4}$ cm^2 V^{-1} s^{-1}, $\mu_h = 6.62 \times 10^{-4}$ cm^2 V^{-1} s^{-1}, and μ_e/μ_h = 0.90). Devices incorporating 4F and 4Cl achieved well-balanced charge transport (μ_e/μ_h = 1.04 and 1.06, respectively).

When processed with a CF: CS_2 solvent system, further improvements were observed, with both ternary systems achieving nearly symmetric and elevated mobilities: for D18/L8-BO:4F, $\mu_e = 7.94 \times 10^{-4}$ cm^2 V^{-1} s^{-1}, $\mu_h = 7.86 \times 10^{-4}$ cm^2 V^{-1} s^{-1}, and μ_e/μ_h = 1.03; for D18/L8-BO:4Cl, $\mu_e = 7.28 \times 10^{-4}$ cm^2 V^{-1} s^{-1}, $\mu_h = 7.52 \times 10^{-4}$ cm^2 V^{-1} s^{-1}, and $\mu_e/\mu_h = 0.97$.

To gain deeper insight into the impact of M-Y6 acceptor integration on charge generation and extraction processes in ambient-processed OSCs, photocurrent density (J_{ph}) versus effective voltage (V_{eff}) curves were measured for the optimized binary and ternary devices based on the D18/L8-BO system (Figure S42a). Here, J_{ph} is defined as the difference between the current densities under illumination and in the dark, while V_{eff} represents the difference between the applied voltage and the voltage at which the net current is zero. The exciton dissociation probability (P_{diss}), estimated from the ratio J_{ph}/J_{sat} at high V_{eff} (≈2 V), revealed values of 98.5% for the binary control, 98.9% for D18/L8-BO:4F (CF: CS_2), and 98.3% for D18/L8-BO:4Cl (CF: CS_2), indicating more efficient exciton dissociation upon incorporation of M-Y6 acceptors—particularly 4F.

Similarly, charge collection efficiency (P_{coll}), calculated from the ratio of J_{ph} to J_{sat} at the maximum power point, improved from 90.8% in the control to 92.9% and 91.6% for the 4F- and 4Cl-based ternary devices, respectively. These enhancements reflect the superior charge generation and extraction dynamics enabled by M-Y6 incorporation, in line with the improved J_{SC} and FF values. The details of the related parameters are summarized in Table S22.

Further analysis of the photocurrent generation process was conducted by examining the dependence of J_{SC} on light intensity under optimal conditions (Figure S42b). The power–law relationship ($J_{SC} \propto P^{\alpha}$) yielded α values of 0.986 (control), 0.998 (4F), and 0.995 (4Cl). The near-unity α value for the 4F-based device indicates minimal bimolecular recombination and highly efficient charge sweep-out, consistent with its superior photovoltaic performance.

Overall, these findings underscore the critical role of M-Y6 acceptor integration—particularly BT(BO)-*v*-T(C12)-4F—in enhancing exciton dissociation and balanced charge transport in OSCs fabricated under ambient conditions. These effects are more effectively realized in the LBL architecture, especially when combined with solvent engineering, compared to conventional BHJ blending.

2.6 | Molecular Packing and Orientation Analysis

To investigate the molecular organization and crystallinity of the active layer components, two-dimensional grazing-incidence wide-angle X-ray scattering (2D-GIWAXS) measurements were

16146840, 0, Downloaded from https://advanced.onlinelibrary.wiley.com/doi/10.1002/aenm.202505110 by Sanghuh Memorial Library, Wiley Online Library on [11/03/2026]. See the Terms and Conditions (https://onlinelibrary.wiley.com/terms-and-conditions) on Wiley Online Library for rules of use; OA articles are governed by the applicable Creative Commons License

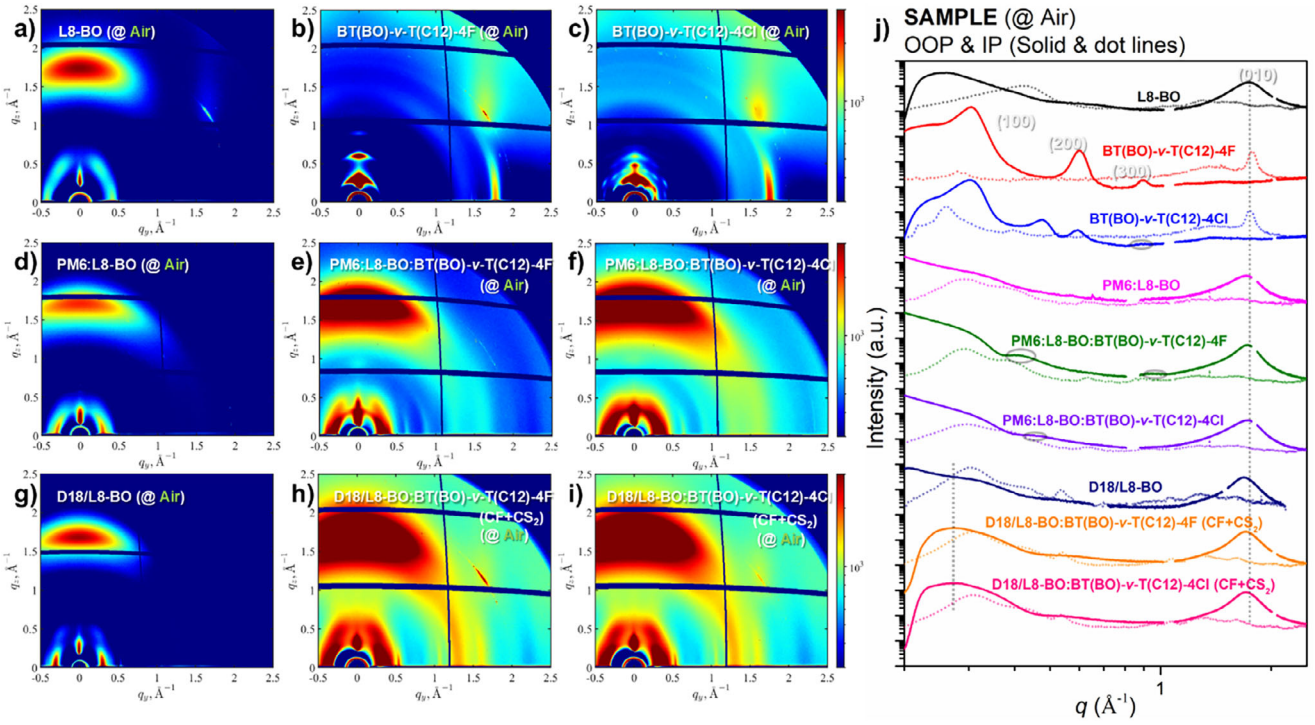

FIGURE 4 | (a–i) 2D-GIWAXS patterns of neat acceptor and binary/ternary blend films based on the BHJ/LBL structure. (j) The out-of-plane (OOP) and in-plane (IP) extracted line-cut-profiles of the corresponding films.

performed under ambient air conditions to better correlate with the device fabrication environment (Figure 4a–i; Figures S43 and S46) [28, 53]. Line-cut profiles were extracted along the out-of-plane (OOP; q_z) and in-plane (IP; q_y) directions (Figure 4j; Figures S44a and S47a). Lamellar ($d_{(100)}$) and π–π stacking ($d_{(010)}$) distances were calculated using Bragg's law, and crystalline coherence lengths (CCLs) were estimated using the Scherrer equation.

To assess molecular orientation, azimuthal intensity ratios (A_y/A_z) were obtained from pole figure plots of the (100) reflections (Figures S44b, S45, S47b, S48, and S49), enabling quantification of face-on versus edge-on stacking. All GIWAXS-derived parameters are summarized in Tables S23–S26.

For pristine donor polymers, GIWAXS analysis revealed that both PM6 and D18 adopt predominantly edge-on orientations, with A_y/A_z values of 0.63 and 0.70, respectively. In contrast, the L8-BO acceptor exhibited strong face-on stacking, as evidenced by a pronounced π–π stacking peak at $q_z = 1.735$ Å^{-1} and a lamellar peak at $q_z = 0.419$ Å^{-1}, yielding an A_y/A_z of 1.18—an orientation favorable for vertical charge transport in photovoltaic devices.

The M-Y6 acceptors displayed markedly different molecular packing behaviors. Both pristine 4F and 4Cl films adopted edge-on-dominant orientations, with A_y/A_z values of 0.03 and 0.16, respectively. Remarkably, 4F exhibited long-range lamellar ordering, characterized by sharp diffraction peaks corresponding to the (100), (200), and (300) planes at $q_z = 0.305$, 0.601, and 0.899 Å^{-1}. These features translated to exceptional corresponding CCLs of 198.21, 134.07, and 106.35 Å—among the highest reported for Y6 derivatives and their analogs [10, 11, 13–19, 38, 39]. Although 4Cl showed a similar diffraction pattern, its lamellar order and CCLs were comparatively lower.

This pronounced crystallinity in M-Y6 acceptors, particularly for 4F, is expected to facilitate efficient charge transport by enabling extended molecular packing pathways and reducing charge-trapping grain boundaries [14, 15, 33].

Binary PM6:M-Y6 blend films exhibited pronounced diffraction signals in both OOP and IP directions, indicative of excessive mixed crystallinity and phase separation. Among them, the PM6:4F blend demonstrated more favorable molecular packing than PM6:4Cl, as reflected by a smaller π–π stacking distance ($d_{(010)} = 3.75$ Å) and a higher face-on orientation ratio ($A_y/A_z = 1.24$), compared to 4.01 Å and 0.42 for PM6:4Cl, respectively. These structural advantages correlate well with the superior device performance of the 4F-based binary OSCs.

Upon incorporating M-Y6 acceptors into BHJ-based ternary blends with PM6:L8-BO, both systems exhibited enhanced molecular ordering, particularly in lamellar and π–π stacking. For example, the PM6:L8-BO:4F ternary blend displayed distinct crystalline peaks at $q_z = 0.410$ and 0.940 Å^{-1}, corresponding to reduced $d_{(100)}$ and $d_{(010)}$ values of 15.32 and 3.63 Å, respectively. Furthermore, its A_y/A_z ratio increased slightly to 0.97, surpassing that of the control blend (3.67 Å and $A_y/A_z = 0.96$), suggesting a more face-on-favorable molecular orientation and denser π–π stacking.

Most notably, the π–π crystalline coherence length ($CCL_{(010)}$) followed the order: control < 4Cl < 4F, mirroring the observed trends in device performance. These results indicate that the introduction of M-Y6 acceptors, especially 4F, into ternary

16146840, 0, Downloaded from https://advanced.onlinelibrary.wiley.com/doi/10.1002/aenm.202505110 by Sanghuh Memorial Library, Wiley Online Library on [11/03/2026]. See the Terms and Conditions (https://onlinelibrary.wiley.com/terms-and-conditions) on Wiley Online Library for rules of use; OA articles are governed by the applicable Creative Commons License

systems promotes improved molecular organization and packing density, which contribute to enhanced charge transport and photovoltaic efficiency.

Similarly, in the optimized LBL-based ternary films processed with a CF: CS_2 (8:2 v/v) co-solvent system, the structural contributions of M-Y6 acceptors were further magnified. The D18/L8-BO:4F blend exhibited improved molecular ordering, with $d_{(100)}$ = 22.93 Å, $CCL_{(100)}$ =63.54 Å, $d_{(010)}$ = 3.68 Å, and $CCL_{(010)}$ = 26.06 Å. In comparison, the 4Cl-based blend showed slightly broader packing ($d_{(100)}$ = 22.93 Å, $CCL_{(100)}$ = 54.42 Å, $d_{(010)}$ = 3.68 Å, and $CCL_{(010)}$ = 25.86 Å), yet both outperformed the control D18/L8-BO film ($d_{(100)}$ = 25.44 Å, $CCL_{(100)}$ = 35.03 Å, $d_{(010)}$ = 3.72 Å, and $CCL_{(010)}$ = 23.27 Å). These data collectively indicate denser π–π stacking and enhanced long-range ordering upon incorporation of M-Y6 acceptors.

Orientation analysis further supported these findings. The A_y/A_z ratios of 1.36 (4F) and 1.24 (4Cl) represent a more balanced molecular orientation compared to the higher value of 1.55 in the control, which is often associated with excessive face-on preference and suboptimal vertical transport [8, 54, 55].

These GIWAXS results emphasize the dual structural merits of M-Y6 acceptors: intrinsic high crystallinity and tunable molecular orientation. When combined with a LBL blend strategy and appropriate solvent engineering, these features drive the formation of favorable packing motifs and robust phase behavior. These structural attributes directly correlate with the superior device performance and reliability observed in ambient-air-fabricated OSCs.

2.7 | Morphology Analysis

To elucidate the structure–performance relationships in air-processed OSCs based on M-Y6 acceptors, the surface and bulk morphologies of the active layers were investigated using atomic force microscopy (AFM) and high-resolution transmission electron microscopy (HR-TEM), as shown in Figure 5a–f and Figures S50–S52. All films were processed under conditions identical to those used for device fabrication. Root-mean-square (RMS) roughness values were extracted from AFM height images to assess surface uniformity, while phase images provided insights into domain distribution and phase separation in binary and ternary blends [28, 31, 53].

As shown in Figure S50, the PM6:4F binary film exhibited a relatively smooth morphology (RMS = 1.32 nm) with finely distributed nanoscale features—supporting efficient donor–acceptor phase separation and charge transport [38, 56]. In contrast, the PM6:4Cl film displayed larger domains and a rougher surface (RMS = 1.71 nm), indicating suboptimal phase morphology, consistent with its inferior device performance. The PM6:L8-BO control showed a well-interconnected, bi-continuous morphology (RMS = 0.80 nm) with finely dispersed domains, characteristic of balanced charge generation and extraction in high-performing BHJ systems (Figure S51a) [48].

Upon incorporation of M-Y6 acceptors into PM6:L8-BO in a BHJ ternary configuration, both 4F- and 4Cl-containing blends exhibited slightly increased RMS values (0.91 and 0.94 nm, respectively), suggesting enhanced phase separation and refined domain features (Figure S51b,c) [31]. Notably, the 4F-based ternary blend exhibited pronounced nanofibrillar textures—attributable to the high crystallinity of BT(BO)-*v*-T(C12)-4F—which likely facilitate continuous percolation pathways for charge carriers. This morphology correlates with the enhanced J_{SC} and FF observed in corresponding BHJ-based ternary devices [7, 17, 28].

As shown in Figure 5a–c and Figure S52, in the LBL-processed D18/L8-BO system, the binary control exhibited a well-defined fibrillar network (RMS = 0.90 nm), conducive to anisotropic charge transport. Introducing M-Y6 acceptors under CF: CS_2 (8:2 v/v) solvent processing further optimized the morphology. The D18/L8-BO:4F ternary film presented a uniform nanofibrillar network with a slightly increased RMS (0.95 nm), indicative of enhanced ordering and favorable phase separation for efficient charge extraction [7, 9, 28]. In contrast, the 4Cl-based ternary film, although slightly smoother (RMS = 0.76 nm), showed excessive phase separation and morphological irregularities, which may disrupt charge continuity and promote recombination [28, 31].

These observations were corroborated by HR-TEM analysis (Figure 5d–f), which revealed that the D18/L8-BO control film had a homogeneous and smooth texture, while the 4F-based ternary film exhibited hierarchical, wrinkled nanofibrils—features known to enhance optical scattering and light trapping, thereby improving photocurrent generation [5, 9]. Conversely, the 4Cl-based film showed disordered fibrillar morphology with large, ill-defined domains, indicative of morphological instability and inefficient charge transport pathways [28, 31].

Collectively, these findings underscore the critical role of M-Y6 acceptors in regulating active layer morphology under ambient-air conditions. In particular, the inclusion of highly crystalline 4F facilitates the formation of well-ordered nanofibrillar networks and favorable nanoscale phase separation—key attributes for achieving efficient exciton dissociation, directional charge transport, and ultimately, high-performance OSCs.

2.8 | Miscibility, Crystallinity, and Scalability Factor Analysis

To elucidate the morphological evolution and phase behavior of air-processed active layers, contact angle measurements were performed to assess the miscibility and interfacial compatibility of donor and acceptor components [23, 25, 32, 33, 38, 39, 42, 44, 56]. As shown in Figure 6a and Figure S53, contact angles of water and diiodomethane (DIM) were measured on thin films of PM6, D18, L8-BO, M-Y6 acceptors, and dual-acceptor blends. Surface energies (γ), including polar and dispersive components, were calculated using Wu's method (Table S27).

Both M-Y6 acceptors exhibited significantly higher water contact—106.49° for 4F and 103.43° for 4Cl—compared to 94.49° for L8-BO, indicating their more hydrophobic nature. The surface energies derived from contact angles were 30.52 mN m^{-1} for 4F and 34.68 mN m^{-1} for 4Cl, closely matching those of PM6 (34.23 mN m^{-1}) and D18 (33.16 mN m^{-1}). These similarities

16146840, 0, Downloaded from https://advanced.onlinelibrary.wiley.com/doi/10.1002/aenm.202505110 by Sanghuh Memorial Library, Wiley Online Library on [11/03/2026]. See the Terms and Conditions (https://onlinelibrary.wiley.com/terms-and-conditions) on Wiley Online Library for rules of use; OA articles are governed by the applicable Creative Commons License

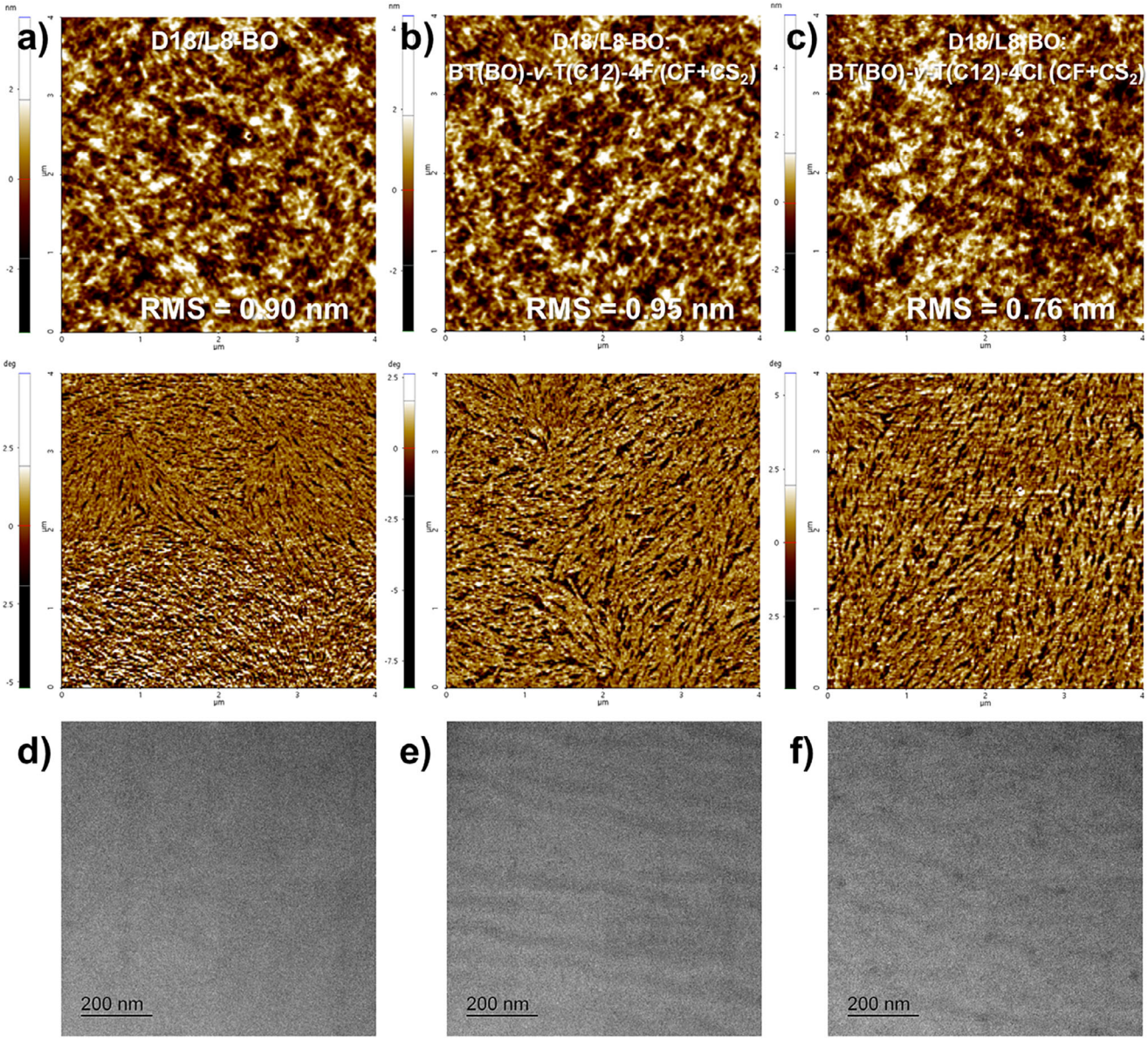

FIGURE 5 | (a–c) AFM height and phase images (4 μm × 4 μm), along with (d–f) HR-TEM images images of the optimized air-processed binary and ternary blend films (LBL) utilizing a mixed CF: CS_2 co-solvent system: D18/L8-BO, D18/L8-BO: BT(BO)-*v*-T(C12)-4F (CF + CS_2), and D18/L8-BO: BT(BO)-*v*-T(C12)-4Cl (CF + CS_2).

suggest favorable miscibility and interfacial compatibility between the M-Y6 acceptors and donor polymers.

To quantitatively evaluate thermodynamic interactions, Flory–Huggins interaction parameters (χ) were estimated based on the calculated surface energies (Table S28) [38, 39, 50, 56]. Lower χ values denote improved miscibility [42]. The binary PM6:L8-BO and D18/L8-BO systems showed χ values of 0.400K and 0.526K, respectively. Upon M-Y6 incorporation, χ values markedly decreased: in BHJ systems, χ dropped to 0.206K (4F) and 0.292K (4Cl); in LBL systems, values were 0.298K (4F) and 0.400K (4Cl). These results confirm that the introduction of M-Y6 acceptors enhances miscibility and molecular compatibility across both BHJ and LBL configurations.

Interestingly, the performance impact of M-Y6 acceptors was more pronounced in LBL-based OSCs than in BHJ-based systems. In BHJ architectures, which consist of a single, uniformly mixed phase, the high hydrophobicity and low surface energy of M-Y6 acceptors—closely resembling those of the donor polymers—can lead to overmixing. This excessive miscibility may hinder optimal phase separation, reduce domain purity, and compromise percolation pathways, ultimately limiting charge transport and device efficiency [38, 39, 56].

In contrast, the LBL strategy, which inherently introduces vertical stratification and sequentially processed interfaces, allows M-Y6 acceptors to act as effective morphological modulators. Their incorporation enables controlled interdiffusion at the donor

16146840, 0, Downloaded from https://advanced.onlinelibrary.wiley.com/doi/10.1002/aenm.202505110 by Sanghuh Memorial Library, Wiley Online Library on [11/03/2026]. See the Terms and Conditions (https://onlinelibrary.wiley.com/terms-and-conditions) on Wiley Online Library for rules of use; OA articles are governed by the applicable Creative Commons License

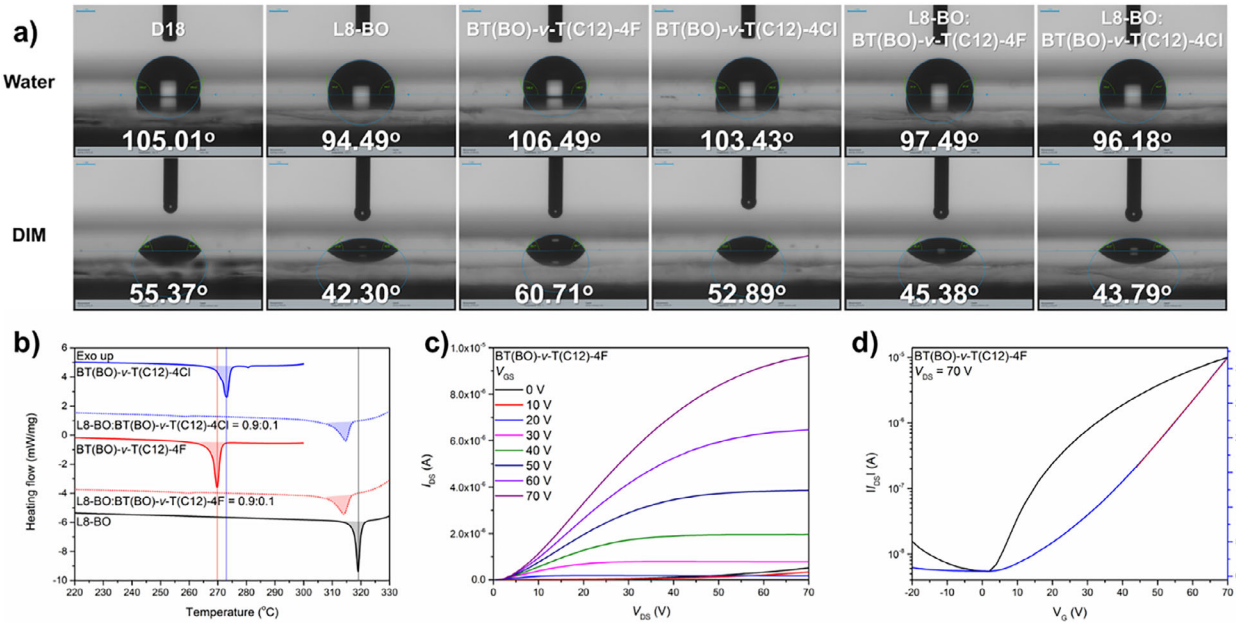

FIGURE 6 | (a) Contact angles and (b) DSC curves of neat donor/acceptor and two-acceptor films. (c) Output and transfer characteristics of the optimized organic field-effect transistors (OFETs) based on BT(BO)-*v*-T(C12)-4F, which were annealed at 200°C and processed under ambient air conditions.

–acceptor interface, fostering favorable nanoscale phase separation and suppressing recombination. This structured phase behavior enhances exciton generation, dissociation, and directional charge transport. Consequently, LBL-based devices incorporating M-Y6 acceptors exhibited significantly improved performance under ambient-air processing—highlighting the synergistic role of material design and fabrication strategy in achieving scalable, high-efficiency OSCs [7, 45].

To further explore how miscibility influences crystallinity in air-processed OSCs, DSC was conducted on neat donor polymers, binary/ternary blends, and dual-acceptor systems (Figure 6b; Figures S54–S57). As expected, the neat donor polymers PM6 and D18 exhibited no thermal transitions, confirming their amorphous nature. In contrast, as mentioned earlier, the pristine M-Y6 acceptors displayed sharp melting peaks, indicative of their semi-crystalline character, with ΔH_m values of −39.3 J g^{-1} (4F) and −37.4 J g^{-1} (4Cl).

Upon blending with PM6, both PM6:4F and PM6:4Cl binary systems exhibited substantial reductions in melting enthalpy (−11 and −7.7 J g^{-1}, respectively), reflecting a significant loss of crystallinity (Figure S54). These observations are consistent with their low Flory–Huggins interaction parameters (χ = 0.106K for PM6:4F and 0.001K for PM6:4Cl; Table S28), suggesting excessive miscibility that leads to overmixing and suppressed molecular ordering. Such excessive blending can disrupt phase purity, thereby impeding optimal charge transport and reducing photovoltaic performance.

Interestingly, when M-Y6 acceptors were introduced into PM6:L8-BO ternary systems in a BHJ configuration, the crystallinity of the active layer was partially restored. Ternary blends exhibited intermediate ΔH_m values (−16.2 J g^{-1} for 4F and −13.1 J g^{-1} for 4Cl), compared to the PM6:L8-BO control (−19.6 J g^{-1}), indicating a more balanced interplay between miscibility and crystallization (Figure S55). This suggests that the presence of L8-BO acts as a morphological regulator, mitigating the excessive miscibility of M-Y6 with the donor polymer [38, 39, 56].

In D18-based systems, similarly low χ values (0.055K for D18:4F and 0.017K for D18:4Cl; Table S28) also implied high miscibility. However, LBL-processed ternary blends provided a structurally advantageous configuration. The spatially distinct donor–acceptor interfaces inherent to the LBL architecture help preserve molecular ordering by reducing intermixing. This structural segregation enhances crystallinity and supports efficient exciton dissociation and charge transport, directly translating to improved device performance [7, 45, 57].

At the optimal L8-BO: M-Y6 blend ratio of 0.9:0.1 (w/w), DSC thermograms revealed alloy-like behavior with major melting transitions dominated by L8-BO ($T_m \approx 314$°C; ΔH_m = −35.94 J g^{-1} for 4F and −34.16 J g^{-1} for 4Cl; Figure 6b) [10]. Minor melting peaks from the M-Y6 components were also observed at lower temperatures (259.6°C/−1.82 J g^{-1} for 4F; 258.1°C/−1.26 J g^{-1} for 4Cl), suggesting partial miscibility and the formation of mixed crystalline domains [10, 57]. These thermal signatures are consistent with the hierarchical molecular packing observed in GIWAXS analysis.

Importantly, the calculated χ values at a 1:1 blend ratio (0.920K for 4F: L8-BO and 0.354K for 4Cl: L8-BO; Table S28) were significantly higher than those at 0.9:0.1, indicating limited miscibility at higher M-Y6 content. This limited compatibility fosters discrete phase separation and enhances domain purity—attributes that are particularly beneficial in LBL architectures, where vertically stratified donor and acceptor domains favor directional charge transport and reduced recombination [7, 45].

16146840, 0, Downloaded from https://advanced.onlinelibrary.wiley.com/doi/10.1002/aenm.202505110 by Sanghuh Memorial Library, Wiley Online Library on [11/03/2026]. See the Terms and Conditions (https://onlinelibrary.wiley.com/terms-and-conditions) on Wiley Online Library for rules of use; OA articles are governed by the applicable Creative Commons License

However, when the M-Y6 concentration was increased to 0.8:0.2, DSC traces showed stronger, distinct melting transitions for individual components, signaling reduced miscibility and excessive phase separation (Figure S57). This morphological instability correlated with decreased device performance in BHJ-based OSCs (Tables S9 and S10), underscoring the critical need to finely tune donor–acceptor miscibility and crystallinity. Achieving this delicate balance is essential for controlling phase behavior, optimizing nanoscale morphology, and realizing high-efficiency OSCs fabricated under ambient conditions.

To gain deeper insights into the origin of enhanced charge transport and device performance in air-processed ternary OSCs, we investigated the intrinsic electron-transport properties of M-Y6 acceptors using organic field-effect transistors (OFETs) [8, 14, 33, 58, 59]. Devices were fabricated in a bottom-gate, bottom-contact (BGBC) configuration under ambient conditions, followed by thermal annealing above 150°C to promote molecular ordering and crystallinity—a prerequisite for effective field-effect transport. All BGBC devices exhibited clear n-type behavior with well-defined saturation regimes, as shown in Figure 6c,d and Figure S58a,b. Among them, BT(BO)-*v*-T(C12)-4F demonstrated the highest field-effect performance when annealed at 200°C, achieving a saturation mobility (μ_{sat}) of 2×10^{-2} cm^2 V^{-1} s^{-1} and a threshold voltage (V_{th}) of 18.1 V. In comparison, BT(BO)-*v*-T(C12)-4Cl exhibited a slightly lower μs_{at} of 1.3×10^{-2} cm^2 V^{-1} s^{-1} and V_{th} of 20.5 V, reflecting its relatively less ordered microstructure. Notably, L8-BO showed negligible current modulation, confirming its poor electron-transport characteristics under the same conditions.

These results clearly establish the intrinsically superior electron mobility of M-Y6 acceptors, particularly 4F, which is consistent with their high crystallinity and well-ordered molecular packing observed in GIWAXS and DSC analyses. This favorable transport behavior contributes directly to the efficient and balanced charge transport observed in both BHJ and LBL ternary OSCs. Furthermore, the ability of M-Y6 acceptors to retain high mobility under air- processing conditions reinforces their potential as robust and scalable acceptor materials for next-generation OSCs. Key OFET performance parameters are summarized in Table S29.

To evaluate the scalability potential of M-Y6 acceptors, we calculated the synthetic scalability factor (SF), defined as the sum of synthetic steps and the inverse of the overall yield [21, 53, 59]. As summarized in Figures S59–S69 and Table S30, both BT(BO)-*v*-T(C12)-4F and BT(BO)-*v*-T(C12)-4Cl exhibited notably low SF values of 31.24 and 24.84, respectively—comparable to leading state-of-the-art low-synthetic complexity NFAs [13, 17–19, 21]. These values reflect the streamlined synthetic routes of M-Y6 acceptors, highlighting their practical potential for material production and integration into device fabrication workflows.

While M-Y6 acceptors show moderate performance in binary OSCs, their integration into ternary systems significantly boosts device efficiency and stability. Ambient-air-fabricated OSCs incorporating M-Y6 achieved PCEs of up to 18.6% using a CF: CS_2 co-solvent system in an LBL architecture. Further improvements with a PEDOT: PSS/Cl-2PACz bilayer HTL yielded average PCEs of ~18.9% (RH 33–65%), with a certified champion device reaching 19%—among the highest for fully air-processed conventional OSCs (Table S31 and Figure S70) [6, 22–25, 46–50].

Collectively, these findings emphasize the dual advantages of M-Y6 acceptors: (i) inherently low synthetic complexity that facilitates streamlined molecular design and (ii) high structural compatibility with ternary systems that drive performance gains under scalable, air-processable conditions.

2.9 | Energy Loss Analysis and Stability Evaluation

To understand the origin of the high V_{OC} and the efficiency improvements enabled by M-Y6 acceptor integration, we conducted a detailed energy loss (E_{loss}) analysis on binary and ternary devices (Figures S71–S72 and Table S32). The total E_{loss} can be expressed as follows: $E_{loss} = \Delta E_1 + \Delta E_2 + \Delta E_3$, where ΔE_1 originates from radiative recombination above the photovoltaic bandgap (E_g^{pv}) due to the Shockley–Queisser limit. ΔE_2 is radiative recombination below E_g^{pv}, and ΔE_3 is nonradiative recombination [17, 60].

The M-Y6 acceptor-based devices (PM6:4F and PM6:4Cl) exhibit larger E_g^{pv}s (1.476 and 1.475 eV) compared with the PM6:L8-BO reference (1.424 eV), which, in accordance with the energy-gap law, enables a higher V_{OC} despite larger ΔE_2 and ΔE_3 contributions. For instance, PM6:4F achieves a V_{OC} of 0.878 V—higher than PM6:L8-BO (0.870 V)—suggesting that the broader optical gap offsets the elevated radiative and non-radiative recombination losses [60].

However, despite the moderate V_{OC} values obtained in PM6:M-Y6 systems, the BHJ architecture suffers from enhanced voltage losses—particularly ΔE_3—due to excessive donor–acceptor miscibility and suboptimal phase separation, which limit exciton dissociation and promote recombination. This is corroborated by higher ΔE_3 values in PM6:4Cl and PM6:4F compared to L8-BO, and is further supported by photoluminescence and charge transport results indicating incomplete PL quenching and mobility imbalance. These results highlight a key challenge in BHJ blends involving M-Y6 acceptors: while a larger E_g improves V_{OC}, it also increases the risk of non-radiative voltage loss when morphological control is insufficient.

In contrast, when M-Y6 acceptors are integrated into LBL-structured D18-based ternary devices, the energy loss landscape significantly improves. LBL devices incorporating BT(BO)-*v*-T(C12)-4F not only preserve a low E_g^{pv} but also exhibit minimized ΔE_3 due to well-defined donor–acceptor interfaces, reduced energetic disorder, and enhanced molecular orientation. This structural advantage suppresses non-radiative recombination and facilitates efficient charge extraction, resulting in lower total E_{loss} and superior V_{OC} retention. When paired with solvent engineering (e.g., CF: CS_2), these LBL systems achieve optimized phase purity and vertical stratification, which collectively minimize recombination losses and support the realization of certified PCEs approaching 19% under ambient conditions. Together, these findings underscore the synergistic role of molecular design and processing architecture in mitigating energy loss and enhancing device performance and stability.

16146840, 0, Downloaded from https://advanced.onlinelibrary.wiley.com/doi/10.1002/aenm.202505110 by Sanghuh Memorial Library, Wiley Online Library on [11/03/2026]. See the Terms and Conditions (https://onlinelibrary.wiley.com/terms-and-conditions) on Wiley Online Library for rules of use; OA articles are governed by the applicable Creative Commons License

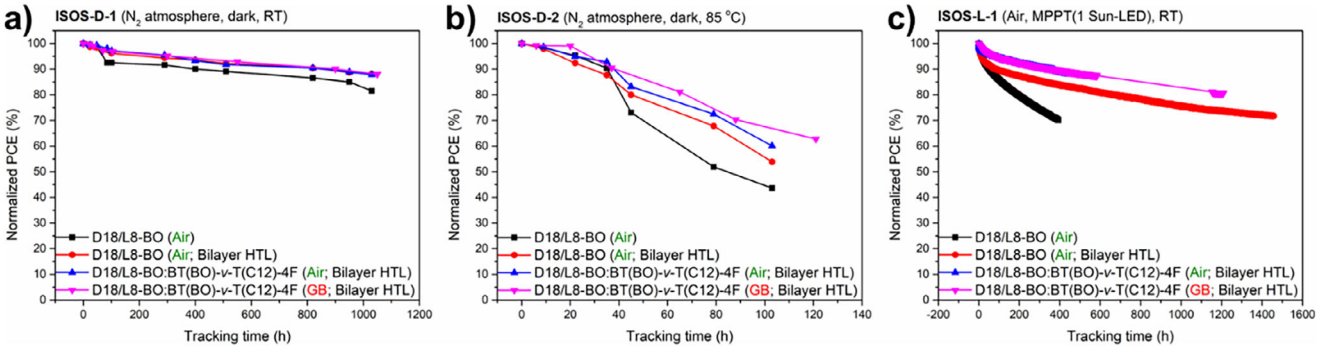

FIGURE 7 | Stability test results of optimized binary and ternary OSCs based on D18/L8-BO system, fabricated under ambient air (Air) and GB (N_2) conditions, evaluated under different ISOS protocols: (a) ISOS-D-1: dark storage in N_2 atmosphere at RT, (b) ISOS-D-2: thermal aging in N_2 atmosphere at 85°C, (c) ISOS-L-1: continous white LED illumination under ambient air with maximum power point tracking (MPPT) at RT. All devices were tested without encapsulation.

To assess the long-term operational viability of the optimized binary and ternary OSCs based on the D18/L8-BO system, we conducted a comprehensive stability evaluation following the International Summit on Organic Photovoltaic Stability (ISOS) protocol, including ISOS-D-1 (dark storage), ISOS-D-2 (thermal stress), and ISOS-L-1 (continuous light exposure) (Figure 7a–c) [60–62]. The detailed information regarding the stability methods is summarized in the Supporting Information. All devices were fabricated either under ambient air (Air) or in a N_2-filled GB, and tested without encapsulation. The configurations studied included a baseline D18/L8-BO binary device, a bilayer HTL-enhanced variant (PEDOT: PSS/Cl-2PACz), and two ternary LBL devices (Air and GB) incorporating BT(BO)-*v*-T(C12)-4F (4F). This systematic comparison provides insights into the environmental robustness of air-processable OSCs under distinct operational stressors such as oxygen/moisture ingress, elevated temperatures, and prolonged photoirradiation.

Under ISOS-D-1 conditions (N_2, dark, RT), the air-fabricated LBL ternary device containing 4F and the bilayer HTL exhibited excellent shelf stability, retaining over 90% of its initial PCE after ~1000 h. In contrast, the standard binary control device showed faster degradation, with only ~80% retention over the same duration. Notably, the LBL ternary device fabricated in the GB showed only marginal improvement over its air-fabricated counterpart, highlighting the intrinsic morphological and chemical robustness of the ternary system even without controlled fabrication conditions—an important consideration for scalable manufacturing.

The thermal stability of the devices was assessed under the ISOS-D-2 protocol (N_2, dark, 85°C), revealing an overall low thermal resilience—a common issue in conventional devices without encapsulation [24, 61, 63]. This degradation is not confined to the photoactive layer but also arises from the thermally induced deterioration of organic interfacial materials such as PEDOT: PSS and PDIN, which have relatively low degradation temperatures. These layers undergo simultaneous thermal stress, accelerating the onset of device failure. Among the tested configurations, the control device exhibited the most rapid and pronounced decline in PCE, indicating severe morphological relaxation and interfacial degradation. In contrast, devices incorporating a bilayer HTL showed significantly improved thermal endurance. Notably, the addition of the highly crystalline 4F acceptor further enhanced thermal durability; the ternary device containing 4F, fabricated under ambient conditions, retained approximately 60% of its initial PCE after 100 h of thermal aging. This improved stability is attributed to the synergistic effects of interfacial engineering and the crystallinity-driven structural robustness of 4F, emphasizing the necessity of stabilizing both interfacial and photoactive layers to effectively mitigate thermal degradation in organic photovoltaic devices.

Under ISOS-L-1 conditions (ambient air, MPPT(1 sun white LED illumination), RT) the binary device with a bilayer HTL exhibited significantly enhanced photostability, retaining ~70% of its initial PCE after 1200 h—substantially outperforming the control, which fell below 70% within 400 h. This improvement is attributed to reduced exciton trapping and suppressed interfacial recombination enabled by the bilayer HTL. Incorporating 4F further enhanced photostability, with both ternary devices—fabricated in air and glovebox—maintaining over 80% of their initial PCEs throughout the test period. This suggests that improved phase stratification and cascade energy alignment in the ternary system effectively suppress photooxidation.

Notably, the similar stability of glovebox- and air-processed 4F-based devices indicates that the enhanced photostability stems from intrinsic material properties and device architecture rather than fabrication conditions. These results underscore the importance of combining highly crystalline acceptors with interfacial engineering to achieve long-term operational stability, supporting the feasibility of ambient-air processing for scalable OSC production. Detailed degradation trends are presented in Figures S73 and S74.

2.10 | Thermodynamically Stable M-Y6 Series (GB vs. Air)

Comprehensive GIWAXS analyses reveal distinct material-dependent differences in crystallinity and molecular orientation among the three non-fullerene acceptors—L8-BO, BT(BO)-*v*-T(C12)-4F (4F), and BT(BO)-*v*-T(C12)-4Cl (4Cl)—as a function of thermal annealing and processing environment (glovebox vs. ambient air; GB vs. Air) (Figure 8a–c and Tables S33–S35)

16146840, 0, Downloaded from https://advanced.onlinelibrary.wiley.com/doi/10.1002/aenm.202505110 by Sanghuh Memorial Library, Wiley Online Library on [11/03/2026]. See the Terms and Conditions (https://onlinelibrary.wiley.com/terms-and-conditions) on Wiley Online Library for rules of use; OA articles are governed by the applicable Creative Commons License

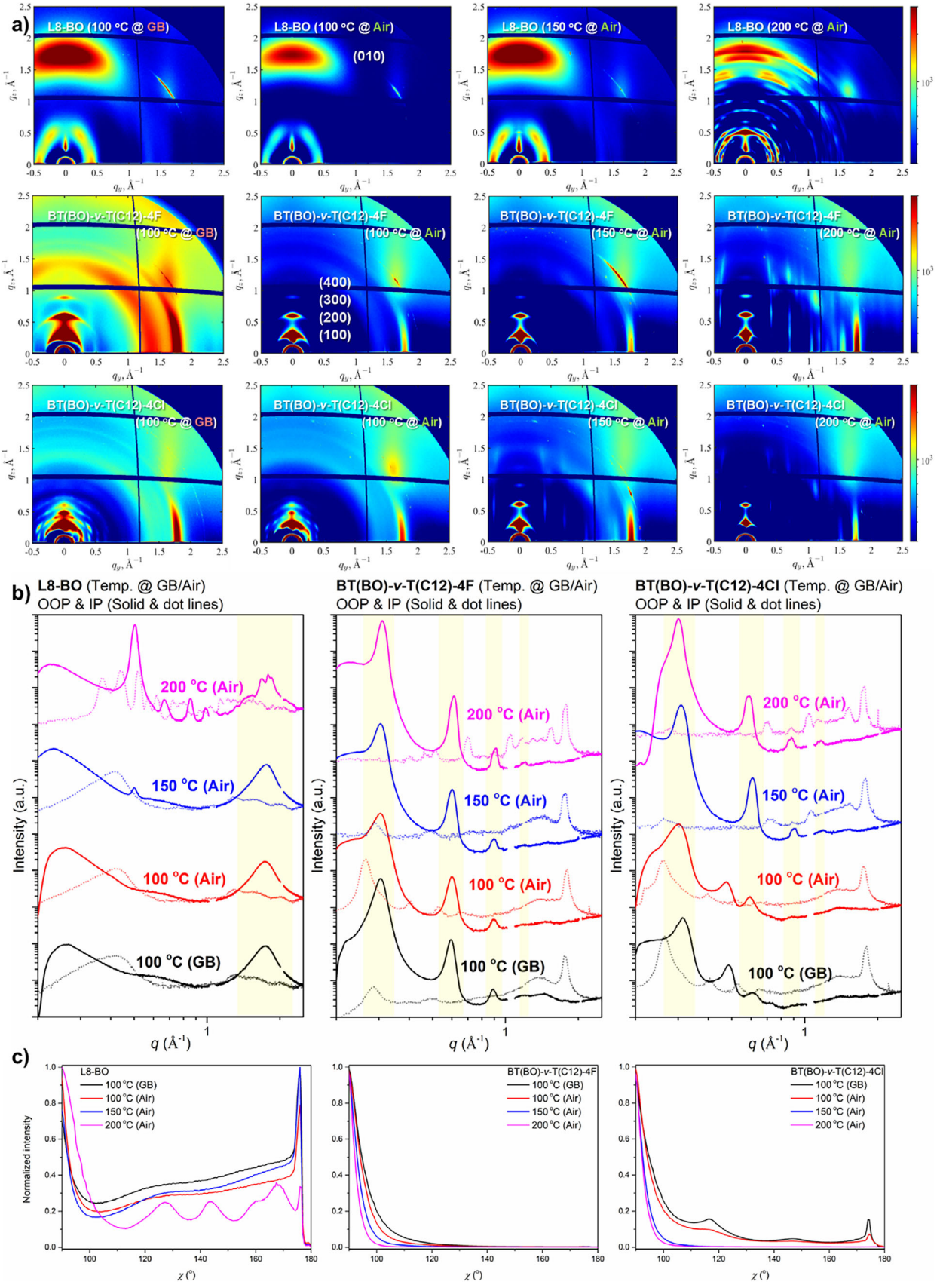

FIGURE 8 | 2D-GIWAXS results of neat acceptor films (L8-BO, BT(BO)-*v*-T(C12)-4F, and BT(BO)-*v*-T(C12)-4Cl) as a function of processing environmental (GB vs. Air) and annealing temperature (100°C, 150°C, and 200°C): (a) 2D-GIWAXS patterns, (b) line-cut-profiles in both the OOP and IP directions, and (c) azimuthal pole figure plots.

16146840, 0, Downloaded from https://advanced.onlinelibrary.wiley.com/doi/10.1002/aenm.202505110 by Sanghuh Memorial Library, Wiley Online Library on [11/03/2026]. See the Terms and Conditions (https://onlinelibrary.wiley.com/terms-and-conditions) on Wiley Online Library for rules of use; OA articles are governed by the applicable Creative Commons License

[14, 47]. Under inert N_2 glovebox conditions, all films display sharp and intense diffraction peaks, indicative of well-ordered thermodynamically stable crystalline phases. However, when processed in ambient air, the presence of oxygen and moisture initially disturbs crystallization, leading to reduced structural order and increased orientational disorder—especially at lower annealing temperatures. Notably, with increasing thermal energy, all materials exhibit progressive structural reorganization and partial to full recovery of their crystalline ordering, with the nature and extent of this recovery being strongly dependent on molecular structure.

For L8-BO, the air-processed film annealed at 100°C shows clear reductions in crystallinity and face-on orientation relative to the glovebox-prepared film, suggesting that the material is highly sensitive to environmental interference during early-stage crystallization. Upon thermal annealing at 150°C, however, L8-BO undergoes significant structural recovery, showing enhanced lamellar (100) and π–π (010) stacking CCLs, along with improved A_y/A_z ratios. This indicates the development of a well-aligned face-on morphology, favorable for vertical charge transport. At 200°C, however, further annealing leads to over-crystallization: although CCLs continue to increase, diffraction peaks broaden, and azimuthal intensity spreads, signaling the onset of polycrystalline domain formation and loss of directional order. This excessive morphological growth is likely detrimental to charge transport and can impair device performance. These findings highlight the narrow thermal processing window for L8-BO and the importance of precise temperature control to balance crystallinity and orientation.

In contrast, both 4F and 4Cl demonstrate robust and thermodynamically favorable structural evolution under ambient air. For 4F, $CCL_{(100)}$ increases markedly from ~198 Å at 100°C to ~273 Å at 200°C, while 4Cl shows a comparable increase from ~148 to ~264 Å. Importantly, the $d_{(100)}$ and $d_{(010)}$ values remain constant or contract slightly, reflecting tighter molecular packing rather than thermally induced disorder. Azimuthal plots further reveal a distinct shift toward edge-on orientation at higher temperatures, as scattering intensity becomes increasingly concentrated along the equator. This orientation evolution is likely driven by the fused-ring backbone and long alkyl chains of the M-Y6 acceptors, which promote thermotropic lamellar stacking and suppress morphological relaxation—even under ambient air exposure.

Finally, GIWAXS data along the OOP direction further support the structural superiority of 4F in dual-acceptor systems (Figures S75–S77 and Table S36). Compared to pristine L8-BO, which has a $CCL_{(010)}$ of 21.34 Å, $d_{(010)}$ of 3.62 Å, and A_y/A_z of 1.18, the 4F-based ternary blend shows significantly enhanced order: $CCL_{(010)}$ increases to 23.96 Å, $d_{(010)}$ contracts to 3.57 Å, and A_y/A_z rises to 1.51. These improvements point to denser π–π stacking and a stronger face-on orientation, both of which are critical for efficient exciton dissociation and vertical charge transport. While the 4Cl-based film also outperforms the control ($CCL_{(010)} = 21.83$ Å, $d_{(010)} = 3.60$ Å, $A_y/A_z = 1.42$), its enhancements are less pronounced—possibly due to the higher dipole moment and steric hindrance introduced by the chlorine substituent, which can slightly disrupt molecular ordering.

To verify the practical viability of the developed materials, we conducted a direct performance comparison between devices fabricated under GB and Air (30%–60% RH) conditions using identical formulations and processing protocols (Table S37). Both binary and ternary systems exhibited high efficiencies under ambient conditions, with the best-performing ternary OSCs (D18/L8-BO:4F) achieving certified PCEs of 19.2% (Air) and 19.1% (GB). Notably, the air-fabricated devices retained over 95% of the glovebox efficiency and exhibited narrower PCE distributions, indicating improved reproducibility. These results highlight the minimal performance trade-off when transitioning to ambient fabrication.

Together, these results underline the structural advantages of 4F, which not only enhances crystalline coherence and molecular orientation but also exhibits high thermal robustness in air. These traits translate directly to the superior photovoltaic performance and stability previously observed in 4F-based OSCs, particularly under ISOS-D-2 and ISOS-L-1 conditions. As such, BT(BO)-*v*-T(C12)-4F emerges as a leading candidate for scalable, ambient-processable OSCs—capable of promoting thermodynamically stable morphologies that enable high device efficiency and long-term operational durability.

3 | Conclusion

In this study, we report the design, synthesis, and comprehensive characterization of two highly crystalline, thermodynamically stable Y6-type acceptors—BT(BO)-*v*-T(C12)-4F (4F) and BT(BO)-*v*-T(C12)-4Cl (4Cl)—and their successful implementation in high-performance, ambient-air-processable OSCs. Through a combination of theoretical modeling, optoelectronic characterization, and advanced morphological analyses, we demonstrate that the incorporation of these M-Y6 derivatives into binary and ternary OSC architectures yields significant improvements in device efficiency, structural order, and long-term operational stability.

From a molecular design perspective, the introduction of a vinylene-linked DA′D core and halogenated IC end groups (4F and 4Cl) affords enhanced planarity, increased dipole moment, and improved π–π stacking capability relative to the benchmark acceptor L8-BO. These modifications promote thermodynamically favorable packing motifs and facilitate strong intermolecular interactions, as confirmed by DFT, ESP, and RDG calculations.

Experimental analyses reveal that the M-Y6 series, particularly 4F, enables superior morphological control even under ambient air processing. GIWAXS results show that while L8-BO exhibits a narrow thermal processing window—prone to disorder at low temperatures and over-crystallization at high temperatures—both 4F and 4Cl maintain or improve crystallinity and molecular orientation with increasing temperature, achieving well-defined lamellar stacking and long-range π–π coherence. The dual-acceptor L8-BO:4F films, in particular, display the highest degree of order, tighter π–π stacking ($d_{(010)}$ = 3.57 Å), and a strongly face-on orientation ($A_y/A_z = 1.51$), which are highly favorable for vertical charge transport.

When integrated into ternary systems using an LBL approach with CF: CS_2 solvent engineering, M-Y6 acceptors significantly

16146840, 0, Downloaded from https://advanced.onlinelibrary.wiley.com/doi/10.1002/aenm.202505110 by Sanghuh Memorial Library, Wiley Online Library on [11/03/2026]. See the Terms and Conditions (https://onlinelibrary.wiley.com/terms-and-conditions) on Wiley Online Library for rules of use; OA articles are governed by the applicable Creative Commons License

enhance morphological stability, exciton dissociation, and charge mobility. These structural advantages result in outstanding device performance, with 4F-based OSCs achieving certified PCEs of 19%—among the highest reported for fully air-processed conventional OSCs. Moreover, systematic stability testing under ISOS-D-1, ISOS-D-2, and ISOS-L-1 protocols confirms the superior thermal and photostability of 4F-containing ternary devices, which retain up to ~80% of their initial PCEs under harsh aging conditions without encapsulation.

In summary, this work establishes BT(BO)-*v*-T(C12)-4F as a next-generation non-fullerene acceptor that combines synthetic scalability, high crystallinity, ambient-processability, and long-term operational durability. The findings underscore the synergistic importance of molecular engineering, interfacial design, and vertical device architecture in overcoming the stability–efficiency trade-off and advancing scalable, high-performance OSC technologies.

Acknowledgements

This paper was supported in part by the Human Resources Development Program of the Korea Institute of Energy Technology Evaluation and Planning (KETEP) grant funded by the Ministry of Trade, Industry and Energy, Republic of Korea (No. RS-2023-00237035). This work was supported by a grant from the Commercialization Promotion Agency for R&D Outcomes (COMPA), funded by the Ministry of Science and ICT, Republic of Korea (No. RS-2023-00304788). E. Cho acknowledges the financial support from the DGIST R&D Program (25-ET-01) of the Ministry of Science and ICT of Korea and the use of the High-Performance Computing (HPC) clusters of the Supercomputing AI Education and Research Center at DGIST.

Conflicts of Interest

The authors declare no conflicts of interest.

Data Availability Statement

The data that support the findings of this study are available from the corresponding author upon reasonable request.

References

1. F. Li, F. R. Lin, and A. K. Y. Jen, "Current State and Future Perspectives of Printable Organic and Perovskite Solar Cells," *Advanced Materials* 36 (2024): 2307161, https://doi.org/10.1002/adma.202307161.

2. S. Feroze, A. Distler, L. Dong, et al., "Long Term Outdoor Performance Evaluation of Printed Semitransparent Organic Photovoltaic Modules for BIPV/BAPV Applications," *Energy & Environmental Science* 18 (2024): 674–688, https://doi.org/10.1039/d4ee04036h.

3. S. Yang, X. Chen, Y. Pan, et al., "High Cell to Module Efficiency Remaining Ratio of ≈90% for the 100 cm 2 Fully Roll-to-Roll Gravure Printed Flexible Organic Solar Cells From Non-Halogenated Solvent," *Advanced Materials* 37 (2025): 2500115, https://doi.org/10.1002/adma.202500115.

4. R. Basu, F. Gumpert, J. Lohbreier, et al., "Large-Area Organic Photovoltaic Modules With 14.5% Certified World Record Efficiency," *Joule* 8 (2024): 970–978, https://doi.org/10.1016/j.joule.2024.02.016.

5. R. Zeng, F. Han, W. Zhong, et al., "Lowering Toxicity of Solvent in Organic Solar Cells Manufacturing for 20% Efficiency," *Advanced Materials* 37 (2025): 2501812, https://doi.org/10.1002/adma.202501812.

6. M. Wen, S. Liu, H. Li, et al., "Ambient Processing of High-Efficiency Organic Solar Modules Enabled by Radical Scavengers," *Angewandte Chemie International Edition* 64 (2025): 202510765, https://doi.org/10.1002/anie.202510765.

7. C. Chen, L. Wang, W. Xia, et al., "Molecular Interaction Induced Dual Fibrils Towards Organic Solar Cells With Certified Efficiency over 20%," *Nature Communications* 15 (2024): 6865, https://doi.org/10.1038/s41467-024-51359-w.

8. J. Deng, W. Li, R. Zeng, et al., "Acceptor Crystallinity Engineering Enables >20% Efficiency Binary Organic Solar Cells With 83% Fill Factor," *Advanced Materials* 37 (2025): 2501243, https://doi.org/10.1002/adma.202501243.

9. L. Zhu, M. Zhang, G. Zhou, et al., "Achieving 20.8% Organic Solar Cells via Additive-Assisted Layer-by-Layer Fabrication With Bulk p-i-n Structure and Improved Optical Management," *Joule* 8 (2024): 3153–3168, https://doi.org/10.1016/j.joule.2024.08.001.

10. M. Zhang, L. Zhu, J. Yan, et al., "Efficient and Stable High-Entropy Organic Photovoltaics," *Joule* 9 (2025): 101851, https://doi.org/10.1016/j.joule.2025.101851.

11. G. Zhang, F. R. Lin, F. Qi, et al., "Renewed Prospects for Organic Photovoltaics," *Chemical Reviews* 122 (2022): 14180–14274, https://doi.org/10.1021/acs.chemrev.1c00955.

12. Q. Jiang, X. Yuan, Y. Li, et al., "A Structurally Simple Polymer Donor Enables High-Efficiency Organic Solar Cells With Minimal Energy Losses," *Angewandte Chemie International Edition* 64 (2025): 202416883, https://doi.org/10.1002/anie.202416883.

13. S. Zhu, C. Shi, Q. Wei, et al., "A-DA ′ D-A Type Pentacyclic Small Molecule Acceptors to Exceed 16.5% Efficiency by Heteroatom Effect at the Outer Side Chain," *Chinese Journal of Chemistry* 41 (2023): 1815–1822, https://doi.org/10.1002/cjoc.202200852.

14. K. H. Huang, C. C. Tseng, C. L. Tsai, et al., "Highly Crystalline Selenium-Substituted C-Shaped Ortho-Benzodipyrrole-Based A-D-A-Type Nonfullerene Acceptor Enabling Solution-Processed Single-Crystal-Like Thin Films for Air-Stable, High-Mobility N-Type Transistors," *Advanced Functional Materials* 35 (2025): 2419176, https://doi.org/10.1002/adfm.202419176.

15. Y. J. Xue, Z. Y. Lai, H. C. Lu, et al., "Unraveling the Structure–Property–Performance Relationships of Fused-Ring Nonfullerene Acceptors: Toward a C-Shaped Ortho -Benzodipyrrole-Based Acceptor for Highly Efficient Organic Photovoltaics," *Journal of the American Chemical Society* 146 (2024): 833–848, https://doi.org/10.1021/jacs.3c11062.

16. M. Deng, X. Xu, Y. Duan, L. Yu, R. Li, and Q. Peng, "Y-Type Non-Fullerene Acceptors With Outer Branched Side Chains and Inner Cyclohexane Side Chains for 19.36% Efficiency Polymer Solar Cells," *Advanced Materials* 35 (2023): 2210760, https://doi.org/10.1002/adma.202210760d.

17. W. Wei, X. Yuan, J. Zhong, et al., "High-Efficiency Organic Solar Cells From Low-Cost Pentacyclic Fused-Ring Electron Acceptors via Crystal Engineering," *Energy & Environmental Science* 17 (2024): 6627–6639, https://doi.org/10.1039/d4ee02296c.

18. Z. Wang, W. Wei, L. Zeng, et al., "A–DA′D–A-Type Pentacyclic Fused-Ring Electron Acceptors for Efficient Organic Solar Cells," *Chemistry of Materials* 35 (2023): 6932–6942, https://doi.org/10.1021/acs.chemmater.3c01216.

19. X. Xu, Q. Wei, J. Song, et al., "High-performance and Low-Cost Organic Solar Cells Based on Pentacyclic A–DA′D–A Acceptors With Efficiency over 16%," *Journal of Materials Chemistry A* 10 (2022): 24717–24725, https://doi.org/10.1039/d2ta07239d.

20. X. Yang, Y. Shao, S. Wang, et al., "Processability Considerations for Next-Generation Organic Photovoltaic Materials," *Advanced Materials* 37 (2025): 2307863, https://doi.org/10.1002/adma.202307863.

21. M. Moser, A. Wadsworth, N. Gasparini, and I. McCulloch, "Challenges to the Success of Commercial Organic Photovoltaic Products,"

16146840, 0, Downloaded from https://advanced.onlinelibrary.wiley.com/doi/10.1002/aenm.202505110 by Sanghuh Memorial Library, Wiley Online Library on [11/03/2026]. See the Terms and Conditions (https://onlinelibrary.wiley.com/terms-and-conditions) on Wiley Online Library for rules of use; OA articles are governed by the applicable Creative Commons License

Advanced Energy Materials 11 (2021): 2100056, https://doi.org/10.1002/aenm.202100056.

22. S. Rasool and J. Y. Kim, "Prospects of Glove-Box Versus Air-Processed Organic Solar Cells," *Physical Chemistry Chemical Physics* 25 (2023): 19337–19357, https://doi.org/10.1039/d3cp02591h.

23. H. Liu, D. Yuan, H. Jiang, S. Li, L. Zhang, and J. Chen, "Siloxane-Induced Robust Photoactive Materials With High Humidity Tolerance for Ambient Processing of Organic Solar Cells," *Energy & Environmental Science* 16 (2023): 3474–3485, https://doi.org/10.1039/d3ee01393f.

24. H. Liu, X. Xie, L. Zhang, J. Wang, and J. Chen, "Siloxane as Humidity-Resistant and Stabilizing Additive for Ambient-Processed Organic Solar Cells," *Advanced Energy Materials* 15 (2025): 2404679, https://doi.org/10.1002/aenm.202404679.

25. Y. He, W. Miao, T. Hu, et al., "Siloxane Decorated Water-Obstructing Guest for Efficient Air-Processed OSCs," *Advanced Science* 12 (2025): 2412190, https://doi.org/10.1002/advs.202412190.

26. J. Mei, N. C. Heston, S. V. Vasilyeva, and J. R. Reynolds, "A Facile Approach to Defect-Free Vinylene-Linked Benzothiadiazole−Thiophene Low-Bandgap Conjugated Polymers for Organic Electronics," *Macromolecules* 42 (2009): 1482–1487, https://doi.org/10.1021/ma802779m.

27. N. Abuhafez and R. Gramage-Doria, "Boosting the Activity of Mizoroki–Heck Cross-Coupling Reactions With a Supramolecular Palladium Catalyst Favouring Remote Zn···Pyridine Interactions," *Faraday Discussions* 244 (2023): 186–198, https://doi.org/10.1039/d2fd00165a.

28. S. J. Jeon, N. G. Yang, J. Y. Kim, Y. C. Kim, H. S. Lee, and D. K. Moon, "A 3-Fluoropyridine Manipulating the Aggregation and Fibril Network of Donor Polymers for Eco-Friendly Solution-Processed Versatile Organic Solar Cells," *Small* 19 (2023): 2301803, https://doi.org/10.1002/smll.202301803.

29. Y. Asanuma, H. Mori, R. Takahashi, and Y. Nishihara, "Vinylene-Bridged Difluorobenzo[: C] [1,2,5]-Thiadiazole (FBTzE): A New Electron-Deficient Building Block for High-Performance Semiconducting Polymers in Organic Electronics," *Journal of Materials Chemistry C* 7 (2019): 905–916, https://doi.org/10.1039/c8tc05764h.

30. H. Mori, Y. Asanuma, R. Hosogi, and Y. Nishihara, "Synthesis and Solar Cell Applications of Semiconducting Polymers Based on Vinylene-Bridged 5-alkoxy-6-Fluorobenzo[c][1,2,5]Thiadiazole (FOBTzE)[c][1,2,5]Thiadiazole (FOBTzE)," *Polymer Journal* 55 (2023): 405–415, https://doi.org/10.1038/s41428-022-00706-z.

31. S. J. Jeon, Y. H. Kim, I. N. Kim, N. G. Yang, J. H. Yun, and D. K. Moon, "Utilizing 3,4-Ethylenedioxythiophene (EDOT)-Bridged Non-Fullerene Acceptors for Efficient Organic Solar Cells," *Journal of Energy Chemistry* 65 (2022): 194–204, https://doi.org/10.1016/j.jechem.2021.05.032.

32. C. Han, H. Gao, Y. Kan, et al., "Two Completely Non-Fused Ring Acceptors Working in an Alloy-Like Model for Efficient and Stable Organic Solar Cells," *Advanced Energy Materials* 14 (2024): 2304063, https://doi.org/10.1002/aenm.202304063.

33. M. Liu, P. Zhu, S. Lai, et al., "Regulating Molecular Structure of S,N-Heteroacene Non-Fullerene Acceptors to Achieve Efficient Photoelectric Properties †," *Chinese Journal of Chemistry* 43 (2025): 13–22, https://doi.org/10.1002/cjoc.202400699.

34. G. P. Kini, S. J. Jeon, and D. K. Moon, "Design Principles and Synergistic Effects of Chlorination on a Conjugated Backbone for Efficient Organic Photovoltaics: A Critical Review," *Advanced Materials* 32 (2020): 1906175, https://doi.org/10.1002/adma.201906175.

35. K. Liu, Y. Jiang, G. Ran, F. Liu, W. Zhang, and X. Zhu, "8.7% 19.7% Efficiency Binary Organic Solar Cells Achieved by Selective Core Fluorination of Nonfullerene Electron Acceptors," *Joule* 8 (2024): 835–851, https://doi.org/10.1016/j.joule.2024.01.005.

36. G. Zhang, X. K. Chen, J. Xiao, et al., "Delocalization of Exciton and Electron Wavefunction in Non-Fullerene Acceptor Molecules Enables Efficient Organic Solar Cells," *Nature Communications* 11 (2020): 3943, https://doi.org/10.1038/s41467-020-17867-1.

37. G. Kupgan, X. K. Chen, and J. L. Brédas, "Molecular Packing of Non-Fullerene Acceptors for Organic Solar Cells: Distinctive Local Morphology in Y6 vs. ITIC Derivatives," *Materials Today Advances* 11 (2021): 100154, https://doi.org/10.1016/j.mtadv.2021.100154.

38. H. Yang, S. Bao, N. Cui, et al., "Morphology Optimization of the Photoactive Layer Through Crystallinity and Miscibility Regulation for High-Performance Polymer Solar Cells," *Angewandte Chemie International Edition* 62 (2023): 202216338, https://doi.org/10.1002/anie.202216338.

39. G. Yao, Y. Ge, X. Xiao, et al., "Preaggregation in Solution Producing Multiple Crystal Forms of Y6 Corresponding to a Variation of Miscibility in PM6-Based Ternary Solar Cells," *ACS Applied Energy Materials* 5 (2022): 1193–1204, https://doi.org/10.1021/acsaem.1c03578.

40. P. Gopikrishna, H. Choi, D. H. Kim, et al., "Impact of Symmetry-Breaking of Non-Fullerene Acceptors for Efficient and Stable Organic Solar Cells," *Chemical Science* 12 (2021): 14083–14097, https://doi.org/10.1039/d1sc04153c.

41. L. Nian, Y. Kan, K. Gao, et al., "Approaching 16% Efficiency in All-Small-Molecule Organic Solar Cells Based on Ternary Strategy With a Highly Crystalline Acceptor," *Joule* 4 (2020): 2223–2236, https://doi.org/10.1016/j.joule.2020.08.011.

42. M. Jahankhan, D. H. Ryu, D. Lee, et al., "High-Performance and Scalable Large-Area Organic Solar Cells Enabled by Alloy-Like Composite-Induced Optimized Morphology Processed From Non-Halogenated Solvent in Air," *Chemical Engineering Journal* 510 (2025): 161811, https://doi.org/10.1016/j.cej.2025.161811.

43. W. Xu and F. Gao, "The Progress and Prospects of Non-Fullerene Acceptors in Ternary Blend Organic Solar Cells," *Materials Horizons* 5 (2018): 206–221, https://doi.org/10.1039/c7mh00958e.

44. Z. Liu, Y. Fu, J. Wu, et al., "Removable Additive Assists Blade-Coated Large-Area Organic Solar Cell Modules Fabricated With Non-Halogenated Solvents Achieving Efficiency over 16%," *Advanced Functional Materials* 35 (2025): 2401558, https://doi.org/10.1002/adfm.202401558.

45. L. Wen, H. Mao, L. Zhang, et al., "Achieving Desired Pseudo-Planar Heterojunction Organic Solar Cells via Binary-Dilution Strategy," *Advanced Materials* 36 (2024): 2308159, https://doi.org/10.1002/adma.202308159.

46. S. Luo, Y. Dou, X. Shi, et al., "Efficient and Stable Air-Processed Organic Solar Cells Enabled by an Antioxidant Additive," *Advanced Materials* 36 (2024): 2407609, https://doi.org/10.1002/adma.202407609.

47. S. Rasool, J. W. Kim, H. W. Cho, et al., "Morphologically Controlled Efficient Air-Processed Organic Solar Cells From Halogen-Free Solvent System," *Advanced Energy Materials* 13 (2023): 2203452, https://doi.org/10.1002/aenm.202203452.

48. T. Gokulnath, H. Kim, J. Lee, et al., "High Performance Air-Processed Organic Photovoltaic Modules (≈55 cm^2) With an Efficiency of >17.50% by Employing Halogen-Free Solvent Processed Polymer Donors," *Advanced Energy Materials* 13 (2023): 2302538, https://doi.org/10.1002/aenm.202302538.

49. H. Xia, Y. Zhang, K. Liu, et al., "Oligomeric Semiconductors Enable High Efficiency Open Air Processed Organic Solar Cells by Modulating Pre-Aggregation and Crystallization Kinetics," *Energy & Environmental Science* 16 (2023): 6078–6093, https://doi.org/10.1039/d3ee02984k.

50. X. Chen, M. Chen, J. Liang, et al., "Polymer Donor With a Simple Skeleton and Minor Siloxane Decoration Enables 19% Efficiency of Organic Solar Cells," *Advanced Materials* 36 (2024): 2313074, https://doi.org/10.1002/adma.202313074.

51. Y. Guo, G. Han, J. Guo, et al., "Engineering Ultrafast Exciton Dynamics to Boost Organic Photovoltaic Performance," *Energy & Environmental Science* 17 (2024): 8776–8786, https://doi.org/10.1039/d4ee03315a.

52. R. Wang, C. Zhang, Q. Li, Z. Zhang, X. Wang, and M. Xiao, "Charge Separation From an Intra-Moiety Intermediate State in the High-Performance PM6:Y6 Organic Photovoltaic Blend," *Journal of the*

16146840, 0, Downloaded from https://advanced.onlinelibrary.wiley.com/doi/10.1002/aenm.202505110 by Sanghuh Memorial Library, Wiley Online Library on [11/03/2026]. See the Terms and Conditions (https://onlinelibrary.wiley.com/terms-and-conditions) on Wiley Online Library for rules of use; OA articles are governed by the applicable Creative Commons License

American Chemical Society 142 (2020): 12751–12759, https://doi.org/10.1021/jacs.0c04890.

53. S. J. Jeon, Y. C. Kim, J. Y. Kim, et al., "Molecular Design of Cost-Effective Donor Polymers With High Visible Transmission for Eco-Friendly and Efficient Semitransparent Organic Solar Cells," *Chemical Engineering Journal* 472 (2023): 144850, https://doi.org/10.1016/j.cej.2023.144850.

54. M. Gao, C. Sun, Y. Li, et al., "Unraveling the Solution Aggregation Structures and Processing Resiliency of High-Efficiency Organic Photovoltaic Blends," *Advanced Materials* 36 (2024): 2406653, https://doi.org/10.1002/adma.202406653.

55. F. Sun, X. Zheng, T. Hu, et al., "1,5-Diiodocyclooctane: A Cyclane Solvent Additive That Can Extend the Exciton Diffusion Length in Thick Film Organic Solar Cells," *Energy & Environmental Science* 17 (2024): 1916–1930, https://doi.org/10.1039/d3ee04281b.

56. C. Wei, J. Zhang, J. Deng, et al., "Morphology Optimization via Pre-Aggregation and Miscibility Matching in PM6:L8-BO Ternary Organic Solar Cells," *Physical Chemistry Chemical Physics* 26 (2024): 28573–28585, https://doi.org/10.1039/d4cp03206c.

57. K. An, W. Zhong, F. Peng, et al., "Mastering Morphology of Non-Fullerene Acceptors Towards Long-Term Stable Organic Solar Cells," *Nature Communications* 14 (2023): 2688, https://doi.org/10.1038/s41467-023-38306-x.

58. T. Duan, J. Wang, X. Zuo, et al., "Head Surgery of Polycyclic o -Quinones With Cyanated Aromatic Rings Towards High Electron Mobility Acceptors Enables 19.6% Efficiency in Additive-Free Binary Organic Solar Cells," *Energy & Environmental Science* 18 (2025): 3773–3783, https://doi.org/10.1039/d5ee00031a.

59. S. J. Jeon, N. Zhao, Y. Yuan, and Y. Li, "Solution-Processable and Ambient-Stable Highly Conductive p-Type Polymers Derived From Dihydropyrazine and Ethylenedioxythiophene," *Advanced Functional Materials* 35 (2025): 2424664, https://doi.org/10.1002/adfm.202424664.

60. S. Jeong, J. Park, Y. Ji, et al., "Building-Up an Interrelationship Between Isomeric Benzyl Inner Side Chains Within Nonfullerene Acceptors and Isomeric Xylene Solvents for Non-Chlorinated Solvent-Processed Organic Solar Cells," *Journal of Materials Chemistry A* 11 (2023): 4703–4716, https://doi.org/10.1039/d2ta08621b.

61. T. L. H. Mai, S. Jeong, S. Kim, et al., "Over 18.2%-Efficiency Organic Solar Cells With Exceptional Device Stability Enabled by Bay-Area Benzamide-Functionalized Perylene Diimide Interlayer," *Advanced Functional Materials* 33 (2023): 2303386, https://doi.org/10.1002/adfm.202303386.

62. J. Park, S. Kim, W. Kim, Z. Sun, B. Lee, and C. Yang, "Stepwise Volatilization Induced by Nature-Sourced Volatile Solid Additives Improving the Efficiency and Stability of Perovskite Solar Cells," *Energy & Environmental Science* 18 (2025): 6260–6272, https://doi.org/10.1039/d4ee03897e.

63. B. Zou, W. Wu, T. A. Dela Peña, et al., "Step-by-Step Modulation of Crystalline Features and Exciton Kinetics for 19.2% Efficiency Ortho-Xylene Processed Organic Solar Cells," *Nano-Micro Letters* 16 (2024): 30, https://doi.org/10.1007/s40820-023-01241-z.

Supporting Information

Additional supporting information can be found online in the Supporting Information section.

Supporting File: aenm70727-sup-0001-SuppMat.docx.

16146840, 0, Downloaded from https://advanced.onlinelibrary.wiley.com/doi/10.1002/aenm.202505110 by Sanghuh Memorial Library, Wiley Online Library on [11/03/2026]. See the Terms and Conditions (https://onlinelibrary.wiley.com/terms-and-conditions) on Wiley Online Library for rules of use; OA articles are governed by the applicable Creative Commons License